Right-Angled Volume of Alternating Links

A Thesis

submitted to
Indian Institute of Science Education and Research Pune
in partial fulfillment of the requirements for the
BS-MS Dual Degree Programme

by

Anurakti Gupta

Indian Institute of Science Education and Research Pune
Dr. Homi Bhabha Road,
Pashan, Pune 411008, INDIA.

April, 2024

Supervisor: Prof. Abhijit Champanerkar
Co-supervisor: Prof. Rama Mishra

Certificate

This is to certify that this dissertation entitled *Right-Angled Volume of Alternating Links* towards the partial fulfilment of the BS-MS dual degree programme at the Indian Institute of Science Education and Research, Pune represents work carried out by Anurakti Gupta at Indian Institute of Science Education and Research under the supervision of Prof. Abhijit Champanerkar and Prof. Rama Mishra during the academic year 2023-2024.

Prof. Abhijit Champanerkar

Prof. Rama Mishra

Committee:

Prof. Abhijit Champanerkar

Prof. Rama Mishra

Prof. Tejas Kalekar

Declaration

I hereby declare that the matter embodied in the report entitled *Right-Angled Volume of Alternating Links* are the results of the work carried out by me at the Department of Mathematics, Indian Institute of Science Education and Research, Pune, under the supervision of Prof. Abhijit Champanerkar, Professor, Department of Mathematics, College of Staten Island, CUNY, and the co-supervision of Prof. Rama Mishra, Professor, Department of Mathematics, IISER Pune, and the same has not been submitted elsewhere for any other degree. Wherever others contribute, every effort is made to indicate this clearly, with due reference to the literature and acknowledgement of collaborative research and discussions.

Anurakti Gupta

This thesis is dedicated to Gauri

Acknowledgments

I would like to express my gratitude to my supervisors, Prof. Abhijit Champanerkar and Prof. Rama Mishra, for conducting this project in such an interesting way that gave me fascinating insights into the field of geometric topology. I am really grateful for Prof. Champanerkar's guidance and patience with me throughout the project despite the time zone difference. His guidance really made this project a wonderful learning and fulfilling experience. I am thankful for the discussions and guidance from Prof. Mishra. She really helped me get a better understanding of hyperbolic knot theory. I would also like to thank my thesis expert, Prof. Tejas Kalelkar for his guidance and advice throughout the year. I would also like to express my gratitude to the Mathematics Department, and Tumpa Di, IISER Pune for helping me appreciate the beauty of mathematics through various productive discussions. I would like to thank my friends for their constant moral and emotional support for the past year. I would also like to thank my family for their support and encouragement.

The support and the resources provided by PARAM Brahma Facility under the National Supercomputing Mission, Government of India at the Indian Institute of Science Education and Research; Pune are gratefully acknowledged.

We would also like to thank Professor Andrew Poje and the Department of Mathematics, College of Staten Island, CUNY for letting us use computational resources on their computational servers.

Abstract

In a recent paper Champanerkar, Kofman and Purcell defined right-angled volume for prime alternating links as a sum of volumes of an associated collection of hyperbolic right-angled ideal polyhedra which is an invariant of the alternating link. Around the same time Felsner and Rote gave a graph theoretic algorithm to obtain right-angled circle patterns associated to planar graphs.

In this thesis, we extend the Felsner-Rote algorithm to alternating knot and link diagrams by developing graph theoretic analogs of the two moves used to compute right-angled volumes, namely rational reduction and decomposition along prismatic 4-circuits. Using this technique we compute right-angled volume for knots in the alternating knot census up to 17 crossings, and links in the alternating link census up to 14 crossings. In addition, using our methods we extend computations of right-angled volume of weaving knots and links, verify their conjecture on the existence of right-angled knots for alternating knots up to 17 crossings, give a new method to generate volumes of right-angled polyhedra recreating volumes computed by Vesnin and Egorov, and explore volumes of fully augmented link complements.

Contents

Introduction

Alternating knot complements have decomposition into polyhedra, this decomposition may be equivalently realised from the combinatorics of the alternating diagram of the knot. Hence, the hyperbolic geometric structure of the complement is studied using their diagrams. Some hyperbolic knots have complements that decompose into ideal hyperbolic right-angled polyhedra. The right-angled structure may be understood from the alternating diagrams. Champanerkar Kofman Purcell [6] describes a procedure for obtaining right-angled polyhedra decomposition of a link complement from a reduced, twist-reduced, prime alternating diagram of the link. These polyhedra can be equivalently obtained using geometry, topology, and combinatorics, hence their volume is a link-invariant known as the right-angled volume. In this thesis, we develop the graph theoretic analog of the procedure to apply to Tait graphs of links to obtain circle packing of the graph, to compute the right-angled volume. This algorithm for computing circle packings is from the work of Stefan Felsner and Gunter Rote [9].

Outlines of the Chapters

Chapter 1 discusses the right-angled kite embeddings of simple 3-connected graphs, circle packings, and the Koebe-Andreev-Thurston theorem. We discuss the Felsner-Rote algorithm to compute circle packings of a 3-connected simple plane graph G. The contents of this chapter follow [9].

Chapter 2 is an introduction to Hyperbolic geometry, especially in dimensions two and three. We study the upper half plane model of $\mathbb{H}^2$ and $\mathbb{H}^3$ and the isometries of hyperbolic space in dimensions two and three.

Chapter 3 serves as an introduction to hyperbolic knot theory. We discuss the examples of Figure 8-knot and the Borromean rings. The discussions in this chapter follow [16].

Chapter 4 discusses the right-angled polyhedra associated with an alternating hyperbolic link. The chapter discusses the combinatorial construction of Andreev polyhedra from [6].

Chapter 5 includes the algorithms for rational reduction and prismatic 4-circuit decomposition, as well as the right-angled volume calculator algorithm.

Chapter 6 discusses the observations and results of the right-angled volumes of the alternating knot census.

Original Contribution

This thesis is of an expository nature and no claim is made to the originality of any of the results in Chapters 1-4. Chapters 5 and 6 have original programs and computations.

Chapter 1

Right-angled Kite Embeddings

In this chapter, we discuss the circle packings associated with primal-dual circle representations. We then discuss a constructive proof for a version of the Koebe-Andreev-Thurston theorem. This work is due to Stefan Felsner and Günter Rote. [9]. The implementation of the algorithm described in section 1.6 is due to Manfred Scheucher. [17]

1.1 Graphs and their connectedness

A graph $G = (V, E)$ is an ordered pair where the set V is the set of vertices and set E is the set of edges that captures the pairwise relationship between $v, v' \in V$ using an edge $e \in E$. The edges of a graph can be either directed or undirected depending on whether a direction is associated with the edges. An undirected graph G is said to be *simple* if there are no multi-edges i.e. more than one edge between two vertices and loops in G. For this chapter, a graph G will be simple and connected unless mentioned otherwise.

Definition 1.1.1. *A graph that can be embedded in a plane is called planar graph. A plane graph is a planar graph with an embedding in the plane.*

Let G be a plane graph. The connected components of $\mathbb{R}^2 - G$ are called the faces of G and are denoted by $F(G)$.

Definition 1.1.2. *Let G be a plane graph. The dual G' of G is defined to be the graph such that $V'(G') = F(G)$ and an edge e for each pair of faces in G that are adjacent along an edge and a self-loop when the same face appears on both sides of an edge.*

Let G be a connected planar graph. Then the dual of its dual G'' is isomorphic to G i.e., it has the same vertex and edge set. Moreover, it has the same planar embedding as G.

Definition 1.1.3. *Let G be a graph. A vertex v of G is called a cut vertex if $G - v$ is disconnected. An edge e of G is called a cut edge if $G - e$ is disconnected.*

Definition 1.1.4. *A graph G is called k-vertex-connected or k-connected if it contains at least k+1 vertices and does not contain a set of $k-1$ vertices whose removal will disconnect the graph. The vertex connectivity $\kappa(G)$ of G is defined as the largest k such that the graph is k-connected.*

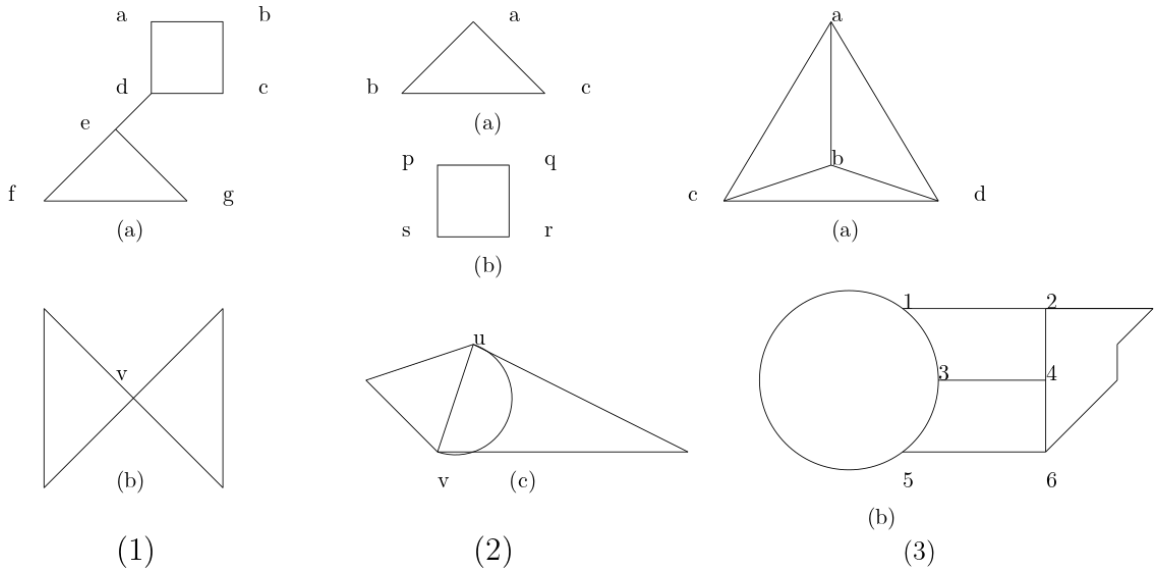

Figure 1.1: Examples of (1) 1-connected graphs, (2) 2-connected graphs, (3) 3-connected graphs. Note that (2) (a), (b) are 2-connected and 1-connected but not 3-connected graphs.

Examples: See Figure 1.1 1) A 0-connected graph is a disconnected graph.
2) A 1-connected graph is the usual connected graph.
3) K_4, the complete graph on 4 vertices is a 3-connected graph.

Note that if a graph G is k-connected, it is also $k-i$ connected, $i \leq k-1$. Hence, in Figure 1.1, (3)(a) and (3)(b) are also 1-connected and 2-connected. On the other hand, (1)(b) is 1-connected but not 2-connected, (2)(c),(2)(b) are 2-connected but not 3-connected.

The components of graph G are its maximal connected sub-graphs. A component (or graph) is trivial if it has no edges; otherwise, it is nontrivial. An isolated vertex is a vertex of degree 0.

Theorem 1.1.1. *Given a 3-connected simple planar graph, its dual graph is also 3-connected, simple and planar.*

Proof. Let G be a 3-connected simple plane graph. Let G' denote the dual graph of G.
First, by the definition of dual graphs, we have that G' is also planar.
Claim: G' is simple. Let's assume to the contrary that G' is not simple, i.e. it has loops and

multiple edges.
Case 1 Let v be a vertex of G' at which there is a loop, this means that the corresponding edge e in G would have been a cut-edge as the faces on both sides of the edge would be the same. This contradicts the 3-connectedness of G as removal of the edge e or two vertices bounding e, will disconnect the graph.
Case 2 Now, if distinct faces of G share an edge then we will get multiple edges in the dual. Again if we remove the endpoints of this edge, the resulting graph is disconnected, thus contradicting the 3-connectedness of graph G.
Claim: G' is 3-connected.
Proof of the claim Let's assume to the contrary that G^* is not 3- connected, so the possibilities for connectivity $\kappa(G^*)$ are $1, 2$.As the dual graph G' is always connected, it will always have $\kappa(G') \geq 1$.
$\kappa(G') = 1$. This would mean that G' is 1-connected and it has cut vertices. So taking a dual of G' would mean that the graph, G'' will have a bunch of loops. But, we have that $G'' = G$ itself, this would contradict the fact that G is 3-connected.
$\kappa(G') = 2$. Again, this would mean that G' is 2-connected, and it has a pair of two vertices whose removal will disconnect the graph. So, taking a dual of G' would result in a loop in G''(=G), but this results in contradiction to the 3-connectedness of G.
In conclusion, we have that G' is 3 vertex-connected. □

For example, in Figure 1.1, for $k = 1$, deletion of vertex v will disconnect the graph into two subgraphs G_1 and G_2.

Definition 1.1.5. *A cut is a partition of the vertices of a graph into two disjoint subsets. Any cut determines a cut-set, the set of edges that have one endpoint in each subset of the partition. These edges are said to cross the cut. A cut $C = (S, T)$ is a partition of V of a graph $G = (V, E)$ into two subsets S and T. The cut-set of a cut $C = (S, T)$ is the set $\{(u, v) \in E \; u \in S, v \in T\}$ of edges that have one endpoint in S and the other endpoint in T.*

For example, in Figure 1.1, for $k = 2$, $\{u, v\}$ forms a cut-set.

We have a special relation for 3-connected simple planar graphs and three-dimensional convex polyhedra.

Theorem 1.1.2. ***Steinitz Theorem*** *A simple graph G is the 1-skeleton of a convex three-dimensional polyhedron if and only if G is planar and 3-connected.*

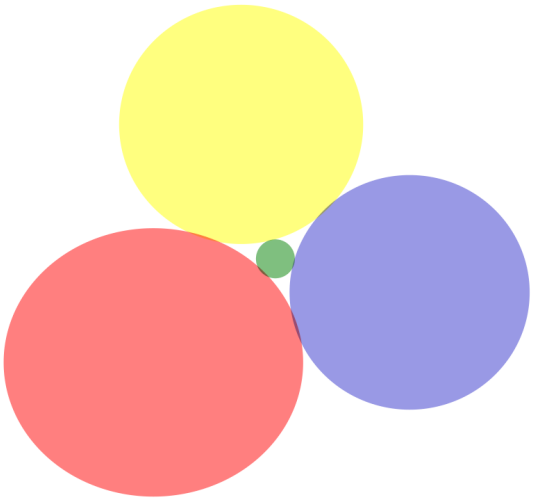

Figure 1.2: A circle packing.

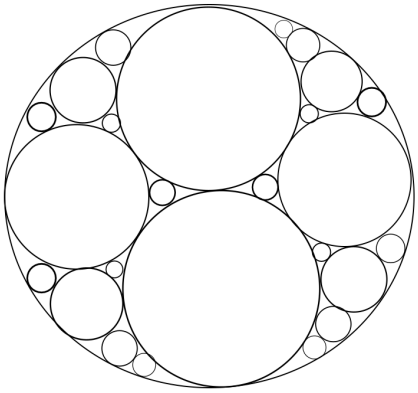

Figure 1.3: An example of an Apollonian circle packing.

1.2 Circle Packings

Definition 1.2.1. *A circle packing is a collection of circles* $\{C_i \mid 1 \leq i \leq n\}$ *in the plane or on* S^2 *such that either* C_i *and* C_j *are either disjoint or touch tangentially for all* i *and* j*.*

Examples One classic example of circle packing is the famous *Apollonian gasket*, see Figure 1.3, which consists of infinitely many circles, where every 3 circles touch each other tangentially. Another example is Figure 1.2

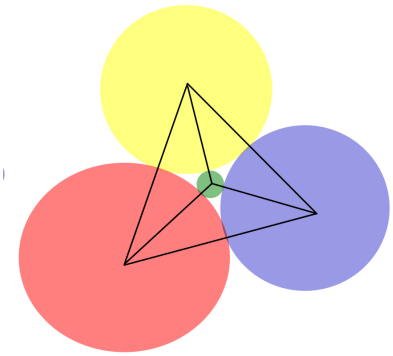

Figure 1.4: Contact(or tangency) graph of the circle packing in Figure 1.2

Definition 1.2.2. *Given a circle packing the contact graph (tangency graph) is a graph whose vertices are represented by circles and whose edges correspond to two tangent circles. See Figure 1.4.*

Koebe, in 1936, proved that every planar graph can be represented as a contact graph of a circle packing [10]. Thurston proved that any triangulation of the sphere has an associated "circle packing," which is unique up to isometries of hyperbolic space [22]. This work was included in the previous works of Andreev and this is collectively known as *Koebe-Andreev-Thurston theorem* which states:

Theorem 1.2.1 (Koebe-Andreev-Thurston Theorem)**.** *For every connected simple planar graph G there exists a circle packing in the plane whose contact graph is G.*

If G is 3-connected simple and planar, we get interesting properties of circle packings for G and its dual G'. Stefan Felsner and Gunter Rote [9] gave constructive proof for a generalization of the Koebe-Andreev–Thurston theorem for 3-connected simple planar graphs. We describe this in the sections below.

1.3 Primal-dual Circle Representations

Let G be a 3-connected simple planar graph embedded on S^2 with vertex set V(G), Edge set E(G) and face set F(G).

Definition 1.3.1. *A spherical primal-dual disk representation consists of two families of disks, $(C_x, x \in V)$ and $(D_y, y \in F)$ on S^2 with the following properties:*

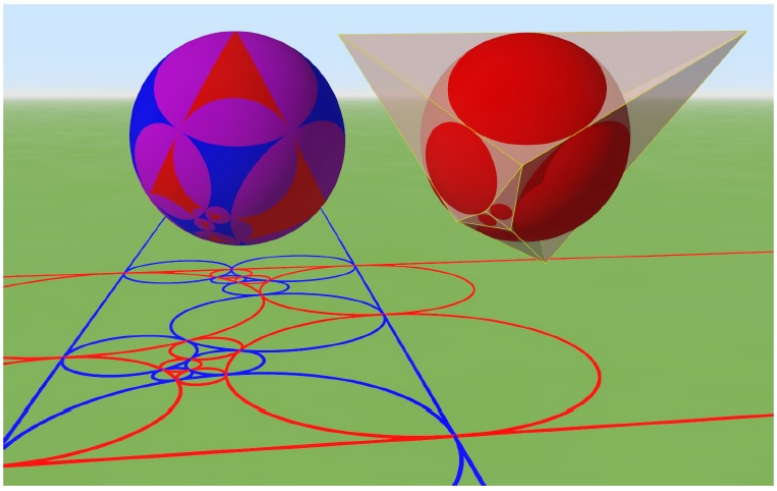

Figure 1.5: Spherical primal-dual disk representation of a graph G on the sphere, primal-dual circle representation on the plane, from [9].

(i) vertex disks C_x have pairwise disjoint interiors.
(ii) face disks D_y have pairwise disjoint interiors. For every edge $xx' \in E$ with dual edge yy', the following holds:
(iii) C_x and $C_{x'}$ are tangent at a point p with common tangent line $t_{xx'}$.
(iv) D_y and $D_{y'}$ are tangent at the same point p with common tangent line $t_{yy'}$.
(v) The lines $t_{xx'}$ and $t_{yy'}$ are orthogonal at p.

A *primal-dual* disk representation of a graph G embedded in the plane is a similar circle packing $\{C_i\}$ and a dual packing $\{D_j\}$ which are orthogonal to each other and whose contact graphs are G and G' respectively. See Figure 1.5.

Theorem 1.3.1. *Every 3-connected simple planar graph G on S^2 admits a primal-dual disk representation on the sphere. This representation is unique up to Möbius transformations.*

We define Möbius transformations later in Chapter 2. As a special case of the theorem 1.3.1 we obtain the classical circle packing theorem:

Theorem 1.3.2. *Every simple plane graph on S^2 admits a circle packing representation, i.e., it is the contact graph of a set of non-overlapping disks in the plane.*

Proof for Theorem 1.3.1 $\implies$ Theorem 1.3.2. First of all, if we have a 3-connected plane graph G, then by theorem 2, we have a primal-dual disk representation of G on the sphere.

Taking stereographic projections of the disks gives a primal-dual circle representation in the plane, thus giving a circle packing representation in the plane.
If we have a plane graph G with connectivity $\kappa(G) \geq 4$, then by definition, it is also 3-connected, and we have a primal-dual disk representation and hence circle packing representations of it.
So, the graphs we have to particularly look at are of two kinds: 2-connected but not 3-connected and graphs which are 1-connected but not 2 or 3-connected. *Case 1* G is 2-connected but not 3-connected.
First, we need to ensure that $|V(G)| \geq 4$, if not we add vertices to make it so. Now, since the graph has cut-sets of size two, we have to eliminate those by adding more edges in the graph ensuring there are no multiple edges, the only condition to maintain is planarity, which is not disturbed in this process. The resulting graph, say H is now 3-connected and we get a circle packing of the graph H. Removing the added vertices will give the circle packing representation of the plane graph G.
Case 2 G is connected but not 2-connected.
Again we have to ensure that $|V(G)| \geq 4$. Once we have that, since the graph has cut vertices we have to get rid of them, so again by keeping the simplicity and planarity of graph G, we add edges to ensure that there are at least two paths between any pair of distinct vertices in G. The resulting graph G' is now 2-connected and we can use Case 1 to get the result. □

Definition 1.3.2. *Let N be a point on S^2. A stereographic projection $\rho : S^2 - N \to \mathbb{R}^2$ maps all but the point N of $\mathbb{S}^2$, called the north pole N bijectively and continuously onto the plane. N serves as the center of the stereographic projection. [19]*

Let $\mathbb{S}^2 = \{(x, y, z)|x^2 + y^2 + z^2 = 1\}$ and $N = (0, 0, 1)$ be the north pole. The plane $z = 0$ runs through the center of the sphere, intersecting at the equator. For a point P (x, y, z) on $\mathbb{S}^2 - \mathbb{N}$, we get a unique line from N passing through P, which intersects the plane $z = 0$ at P' with coordinates (u,v)
$\rho : \mathbb{S}^2 - \mathbb{N} \to \mathbb{R}^2$ *defined as* $\rho(x, y, z) = (\frac{x}{1-z}), \frac{y}{1-z}$.
The inverse map is given as $\rho^{-1} : \mathbb{R}^2 \to \mathbb{S}^2 - \mathbb{N}$ *as*
$\rho^{-1}(u, v) = (\frac{2u}{u^2+v^2+1}, \frac{2v}{u^2+v^2+1}, \frac{u^2+v^2-1}{u^2+v^2+1})$.

An important property of stereographic projections is that they are conformal i.e. they

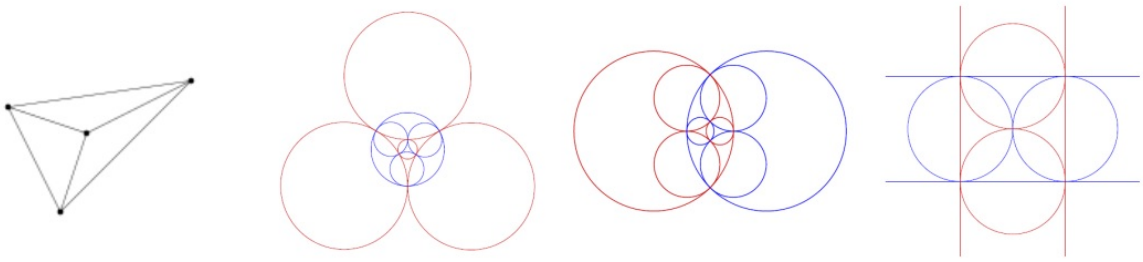

Figure 1.6: Left: K_4 graph; Right: three different primal-dual circle representations of K_4 depending on the center of projection of stereographic projections of primal-dual disk representations of K_4, from [9].

preserve angles [19].

Given a spherical primal-dual circle representation, we can take stereographic projection to get a primal-dual circle representation on the plane, since each circle uniquely bounds a disk, this is the circle packing of G. By changing the pole of the stereographic projections, we get different primal-dual circle representations. See Figure 1.6. Now, we pick a special point as the pole for the stereographic projection.

Definition 1.3.3. *Let G be a 3-connected simple graph on S^2. A cross-centered primal-dual circle representation (CCPDC) of G with central cross $\xi\xi', \eta\eta'$ consists of two vertical lines C_ξ and $C_{\xi'}$, two horizontal lines D_η and $D_{\eta'}$, and two families of circles $(C_x : x \in V - \{\xi, \xi'\})$ and $(D_y : y \in F - \{\eta\eta'\})$ with the following five properties:*
(i) The vertex-circles C_x have pairwise disjoint interiors and are contained in the vertical strip between C_ξ and $C_{\xi'}$.
(ii) The face-circles Dy have pairwise disjoint interiors and are contained in the horizontal strip between D_η and $D_{\eta'}$. Moreover, for every edge $xx' \in E - \xi\xi'$ with dual edge yy', the following holds:
(iii) C_x and $C_{x'}$ are tangent at a point p with common tangent line $t_{xx'}$.
(iv) D_y and $D_{y'}$ are tangent at the same point p with common tangent line $t_{yy'}$.
(v) The lines $t_{xx'}$ and $t_{yy'}$ are orthogonal.

Note that for a 3-connected simple graph G on S^2 with the central cross $\xi\xi', \eta\eta'$, let p be the point of intersection of the circles associated with edges $\xi\xi', \eta\eta'$ in the primal-dual representation of G on S^2. If we pick the point p as the pole of stereographic projection we

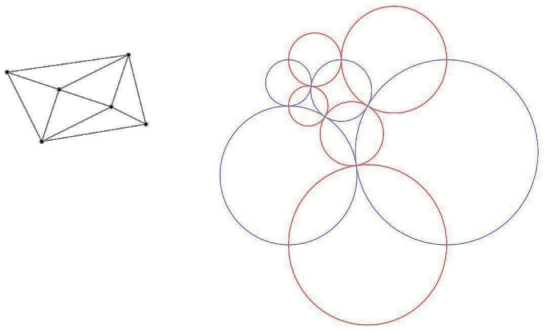

Figure 1.7: A graph G and its associated cross-centered primal dual circle representation, generated using [17].

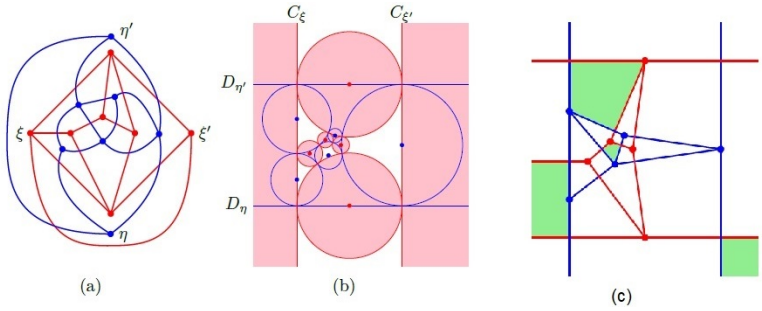

Figure 1.8: (a) A graph G (red) and its dual (blue),(b) cross-centered primal-dual circle representation, (c) Overlaid straight-line drawings of the cross-centred primal-dual circle representation, from [9].

get a cross-centered primal-dual circle representation of G in the plane. See Figure 1.7 The four circles touching at p map to straight lines that are pairwise orthogonal. This results in a rectangle R with the four lines and all other circles are either contained in the rectangle or lying halfway along the sides of R.

We can join the centers of remaining C_x and D_y whenever they are tangent to obtain a decomposition of R into right-angled kites. See Figure 1.8.

Given a 3-connected simple plane graph G, we have the following theorem:

Theorem 1.3.3. *G admits a cross-centered primal-dual circle representation. Moreover, for a given central cross $\xi\xi', \eta\eta'$, this representation is unique up to scaling, translation, and horizontal or vertical reflections. [9]*

Theorem 1.3.1 is accessible from theorem 1.3.3 via inverse stereographic projections.

A brief outline of proof of Theorem 1.3.3: Given a cross-centred primal-dual circle

representation of G. We can use the centres of circle packings of G and G', i.e C_xs and D_ys to get a straight-line drawing of G and G'. Overlaying the two results in the tessellation of the plane into right-angled kites. These kites are uniquely determined by their radii. We start with an initial guess for the radii of the kites obtained and then employ an algorithm to ensure that the angle sum at each vertex is precisely $2 * \pi$. After getting the radii, a special gluing lemma is used to ensure the tiling of the plane by the kites.

1.4 Right-angled Kites

Overlaying the straight-line drawings of G and G' gives the tessellation of the plane into special right-angled kites. Right-angled kites are quadrilateral with two right angles at opposite vertices and a line of symmetry.
In the case of cross-centred primal-dual circle representation, we observe three types of kites. See Figure 1.8.

1. The rectangular strips unbounded in one direction form the *degenerate kites*. They have a vertex with a π angle in the midpoint of the only bounded edge.

2. The four quadrants are regarded as *exceptional kites*.

3. The bounded right-angled kites. These fill the space inside the rectangle.

The collection of kites is in bijection with the collection of pairs (x, x') where x is a primal vertex and x' is the dual vertex. As the corresponding $C_x, C_{x'}$ and $D_y, D_{y'}$ touch orthogonally, the radii completely determine the kites and we have:

For bounded kites, see Figure 1.9:

$$\alpha_{xy} := 2arctan(r_y/r_x) \tag{1.1}$$

$$\alpha_{yx} := 2arctan(r_x/r_y)$$

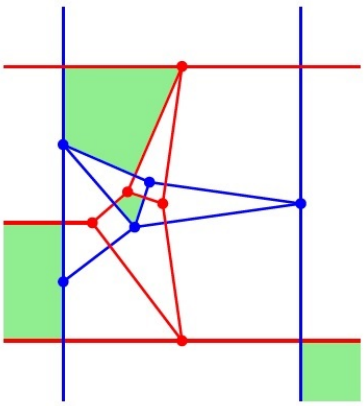

Figure 1.9: Tessellation of the plane into kites, the shaded kites include two bounded kites, one degenerate and one exceptional kite; image from [9].

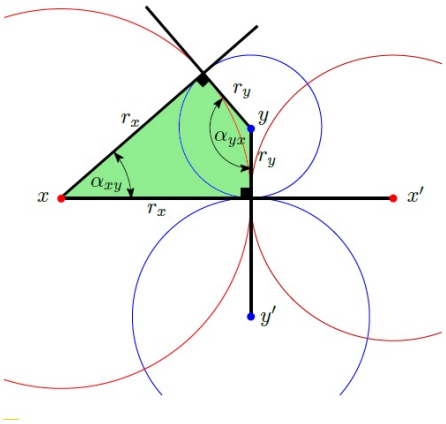

Figure 1.10: The kite corresponding to the pair (x, y), $x \in V(G)$, $y \in F(G)$, from [9].

We can extend to the degenerate kites as follows:

$$\alpha_{uv} = \begin{cases} 0 & r_u = \infty \text{and } r_w \neq \infty \\ \pi & r_w = \infty \text{and } r_u \neq \infty \end{cases} \tag{1.2}$$

Thus, for all (x, y) forming bounded or degenerate kites we have, $\alpha_{xy} + \alpha_{yx} = \pi$. We ignore the exceptional kites in this definition.

The number and combinatorial structure of kites are captured by the angle graph, see Figure 1.10.

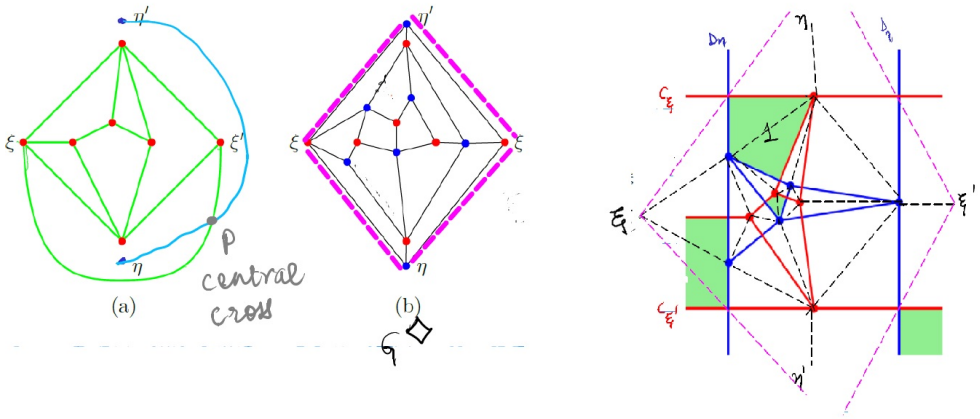

Figure 1.11: Bijection between $G^\diamond$ and right-angled kites, with underlying image from [9].

1.5 Angle Graphs

The angle graph $G^\diamond(U, K)$ of a graph $G = (V, E)$ is a graph with node set $U = V \cup F$ and $K = \{xy, x \in V, y \in F, x \text{ is a vertex on the boundary of face } y\ \}$. $G^\diamond$ is plane and bipartite. The edges of $G^\diamond$ are in bijection with the kites. $G^\diamond$ cannot have a separating 4-cycle. See Figure 1.11.

We set the face corresponding to the edges of the central cross $\xi\eta\xi'\eta'$ as the outer face f_o. The vertices of the outer face form U_o and the edges form K_o. So, we have $U_{in} = U/U_o$ and $K_{in} = K/K_o$. Using Euler's formula for graphs, we have the following lemma for angles graphs :

Lemma 1.5.1. *A simple bipartite plane graph G with $|S| \geq 4$ nodes has at most $|E| \leq |S|-4$ edges, with equality if and only if the graph is connected and every face is a quadrilateral with four distinct vertices.*

Proof. We assume $G = (S, E)$ to be connected, if not we may add some edges to make it connected while ensuring the graph stays bipartite and plane. The resultant graph $G' = (S, E')$ with the face set F. As the graph is bipartite, every face cycle is of even length and contains at least 4 edges, with the only possible exception of a diagonal face cycle, arising from the two sides of a single isolated edge, or two parallel edges. But this is impossible as $|S| \geq 3$ and G is simple connected.

Now, as every edge has 2 sides and every face cycle goes through at least 4 sides of edges,

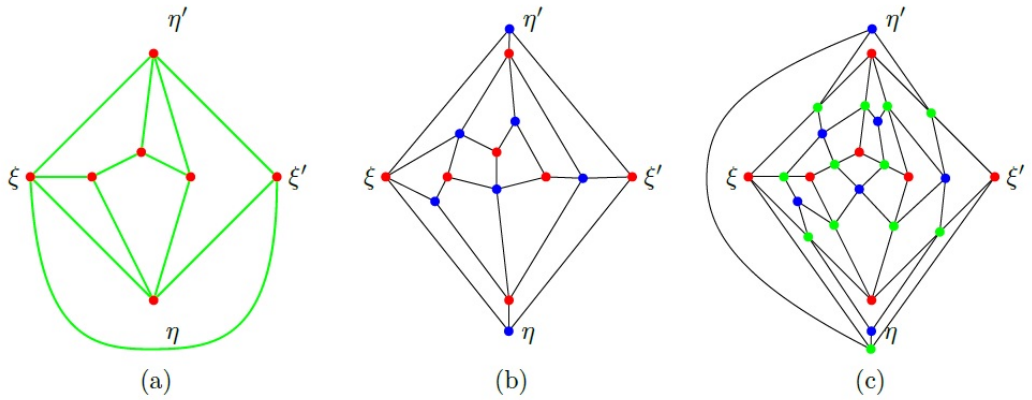

Figure 1.12: (a) A graph G, (b) $G^\diamond$, (c) $(G^\diamond)^\diamond$, The primal-dual completion of G; [9].

therefore $4|F| \leq 2|E'|$. Using Euler's formula, we get that,

$$|E'| + 2 = |S| + |F| \leq \frac{|S| + |E'|}{2}$$

and hence,

$$|E'| \leq 2|S| - 4$$

If all faces $f \in F$ are quadrilateral, the above inequality turns into an equality. And, this is where the connectedness of G' is important because if G were disconnected, $|E| \leq |E'| \leq 2|S| - 4$ will not hold.
Now, we consider the face-cycles of length 4 which do not form a quadrilateral, we note that such a face-cycle could only possibly be the face surrounding a path with two edges, however, this is not possible as $|S| \geq 4$ and G' is connected. □

Now, suppose we have a hypothetical primal-dual circle representation of G that contains a point for each $u \in U_{in}$, which is surrounded by incident kites.

$$\forall u \in U_{in} \text{ we have } \sum_{w:uw \in K} \alpha_{uw} = 2\pi.$$

Now, we assume an arbitrary radius assignment $r : U_{in} \to \mathbb{R}_{\geq 0}$ and we define $r_u = \infty$ for each $u \in U_o$. We can then form the corresponding kites(including the degenerate kites) and get the angles.

Definition 1.5.1. *$\forall u \in U_{in}$ angle sum at u is defined as $\alpha_u = \alpha_u(r) = \sum_{w:uw \in K} \alpha_{uw}$.*

We wish to find a collection of r such that angle sum $\forall u \in U_{in}$ hits the target value 2π. We begin by showing that any choice of radii hit the target angle on average.

Theorem 1.5.2. $\sum_{u \in U_{in}} (\alpha_u(r) - 2\pi) = 0$

Proof.

$$\sum_{u \in U_{in}} \alpha_u(r) = \sum_{uw \in K, u, w \in U_{in}} (\alpha_{uw} + \alpha_{wu}) + \sum_{uw \in K, u \in U_{in}, w \in U_o} \alpha_{uw}$$

As per the definitions of α_{uv}, we get that,

$$= \sum_{uw \in K, u, w \in U_{in}} \pi + \sum_{uw \in K, u \in U_{in}, w \in U_o} \pi = \pi |K/K_o|$$

Now using Lemma 1, as $G^\diamond$ is a simple, connected, bipartite plane graph with more than four vertices and every face is a quadrilateral with four distinct vertices.

$$= \pi(|K| - 4) = \pi(|U| - 8) = 2\pi |U_{in}|$$

□

This means that whenever $\alpha_u(r) \neq 2\pi$, the following both sets are both simultaneously non-empty:

$$U_- = \{u \in U_{in} : \alpha_u(r) \leq 2\pi\} \text{ and } U_+ = \{u \in U_{in} : \alpha_u(r) \geq 2\pi\}$$

If we increase radius r_u at one node $u \in U_+$ leaving the others fixed, by equation (1.1), corresponding to each edge uv, α_{uv} decreases strictly to 0 as $r_u \to \infty$, with the exception of the vertex in U_o with fixed angle π. Therefore, we find that it is possible to increase the value of r_u to ensure that α_{uv} hits 2π.

1.6 Proof of Theorem 1.3.3

We give an algorithm to prove Theorem 1.3.3. The workhorse of the proof is the following iteration:
repeat forever:

for each $u \in U_{in}$:
if $u \in U_+$
increase r_u to reduce $\alpha_u(r)$ to 2π
Claim: Given a random radii assignment, the radii converge to a limiting assignment $\hat{r}_u$ such that $\alpha_{uv}(\hat{r}_u) = 2\pi$ for all edges $uv \in E$.
Proof Since radii can never decrease and the sequence of radii is bounded. As every bounded monotone sequence converges, we need to show that this holds for all nodes $u \in U_{in}$. So, it is enough to show that the set of divergent nodes D is precisely U_o. As $D = \{u \in U : r_u = \infty\}$, and the nodes $u_o \in U_0$ by definition are there in D.
As we increase the radius, the α_{uv} decreases but not below 2π because as we increase the radii the angles at the adjacent nodes increase and jump from U_- to U_+. A jump the other way around is not possible. So, the set U_- is always nonempty until the iteration ends, i.e. $U_+ = \phi$ and $U_- = \phi$. So, we have that U_- is disjoint from D after some time and D is a proper subset of U. Now, we look at the subgraph $G^\diamond$ induced by the nodes in D, denoted by $G^\diamond[D]$. We wish to show that $G^\diamond[D]$ has at least $2|D| - 4$ edges so that we can invoke Lemma 1.5.1. After some time since the initialization of the algorithm, we get that D becomes distinct from U_-. Now,

$$\sum_{u \in D/U_o} \alpha_u(r) \geq \sum_{u \in D/U_o} 2\pi = 2\pi|D/U_o| = 2\pi(D-4) \tag{1.3}$$

And,
if $u \in D$ and $w \in U/D$, $\alpha_{uw} \to 0$. So, in addition to (1.3), the inequality $\alpha_{uw} \leq 1/|U|^2$ will eventually hold for each edge. Bounding these edges separately, we get

$$\begin{aligned}\sum_{u \in D/U_o} \alpha_u(r) &\leq |U|^2.1/|U|^2 + \sum_{\text{kite with} x,y \in D, x \notin U_o or y \notin U_o} (\alpha_{xy} + \alpha_{yx}) \\ &= 1 + \sum_{\text{xy edge of } G^\diamond[D], xy \notin K_o} \pi = 1 + (|E(G^\diamond[D])| - 4)\pi \end{aligned} \tag{1.4}$$

Combining equation 1.3 and 1.4, we get that $|E(G^\diamond[D])| \geq 2|D| - 4$.
Since, $|U_o| \subseteq D$ and $|D| \geq 4$, we have the conditions met to invoke Lemma 1.5.1 and we conclude that $G^\diamond[D]$ is connected and its faces are simple 4-cycles.
The outer face f_o is the cycle formed by nodes of U_o. We wish to show that there is no face other than f_o in $G^\diamond[D]$. Let's assume to the contrary that there is a face $f \in G^\diamond[D]$, which is not a face of $G^\diamond$ which is distinct from f_o. The existence of f is confirmed by the

fact the $G^\diamond[D]$ is a proper subgraph of $G^\diamond$. This face f has to be the inner face of the graph. Since f is distinct from f_o, it would form a separating 4-cycle in $G^\diamond$, which contradicts the 3-connectedness of $G^\diamond$.
This means that all radii r_u for $u \in U_{in}$ converge to limits, $\hat{r}_u$. Hence, all the angles and angle sums converge as well. By the iteration we have $\alpha_u(\hat{r}_u) \leq 2\pi$. By theorem 1.5.2, we get that $\alpha_u(\hat{r}_u) = 2\pi$. %

Theorem 1.6.1. *The radii $\{\hat{r}_u\}$ are unique up to scaling.*

Proof. Let r and r' be two vertices of radii such that $\alpha_r(u) = \alpha_{r'}(u) = 2\pi$, $\forall u \in U_{in}$.
Scaling allows us to assume that $r_{u_o} = r'_{u_o}$ for some $u \in U_{in}$. Consider the set $S = \{u \in U_{in} : r_u > r'_u\}$ and hence $u_o \in U_{in}/S$.

$$|S|.2\pi = \sum_{u \in S} \alpha_u(r) = \sum_{uw \in K.u, w \in S} (\alpha_{uw}(r) + \alpha_{wu}(r)) + \sum_{uw \in K, u \in S, w \in U_o} \alpha_{uw}(r) + \sum_{uw \in K, u, w \in S} \alpha_{uw}(r)$$

$$= \sum_{uw \in K.u, w \in S} 2\pi + \sum_{uw \in K, u \in S, w \in U_o} \pi + \sum_{uw \in K, u, w \in S} \alpha_{uw}(r)$$

The last term has a constant value. If we change radius r to r', the value of $\alpha_{uw}(r)$ in the last term increases. This implies that the set of edges over which sum is taken must be empty. By a symmetrical argument, we get that $S = \{u \in U_{in} : r_u < r'_u\}$ is empty as well.
Thus the radii are unique up to scaling. □

Since the radii uniquely determine the kites the kites can be laid out to form a tessellation of the plane. Hence, we get that the tessellation is unique up to scaling, translation, and horizontal or vertical reflection.

1.7 Tiling a convex polygon

Now that we have all the kites, we wish to lay them out to form the tessellation. The following lemma guarantees the existence of such a tessellation if certain local matching conditions are met:

Lemma 1.7.1. *Let H be a 2-connected plane graph (possibly drawn with curved edges). For each bounded face f of H, a simple polygon P_f is given whose corners are labeled with the*

vertices from the boundary of f in the same cyclic order. Denote the corner of P_f labeled with v by p_{f_v} and the angle of P_f at this corner by β_{f_v}. For each vertex v, let F_v denote the set of incident bounded faces. We assume the following conditions:
(i) $\sum_{f \in F_v} \beta_{f_v} = 2\pi$*, for every inner vertex v.*
(ii) $\sum_{f \in F_v} \beta_{f_v} \leq \pi$*, for every vertex on outer face.*
(iii) $||p_{f_v} - p_{f_w}|| = ||p_{g_v} - p_{g_v}||$ *for every inner edge vw of H with incident faces f and g. Then there is a crossing-free straight-line drawing of H in which every bounded face f can be obtained from P_f by a rigid motion, i.e., translation and rotation.*

Proof. This is a geometric proof involving the induction of the number of interior vertices. We use the fact that a simple polygon can be subdivided into convex pieces by adding diagonals. For induction, we will assume that each polygon P_f is convex and we can do so by dividing the simple polygons into convex pieces, or triangles by inserting diagonals between the vertices. On the other hand, H does not need to be 2-connected, and there may even be multiple edges. However, H still has to be connected and the outer face is a simple 4-cycle. We begin the induction as follows: we pick one vertex $u \in U_{in}$, we take the faces $f_1, f_2, ...f_k$ incident on u, and the corresponding polygons $P_{f_1}, P_{f_2}, ...P_{f_k}$ successively around the origin. By condition (i), we have that these polygons completely surround the origin. Since the polygons are convex, no faces intersect each other and the overall result is a simple polygon P containing u in its interior. Now, we triangulate P. Removing u from H and insert new edges to H, replacing the faces $f_1, f_2, ...f_k$ by the new triangular pieces. This is where possibly multiple edges may be created, however, H still remains connected. While doing this replacement construction, the angle sums $\sum_{f \in F_v} \beta_{f_v}$ remaining same at every vertex v distinct from u, thus conditions (i) and (ii) are met. Also, by construction of the new polygons, shared edge lengths of the adjacent polygons, ensuring condition (iii). The resulting graph H' has one vertex less. By induction, all its faces can be laid out in the plane without overlap with adjacent polygons sharing an edge. The new triangles that were added form a polygon congruent to P. Dividing it into pieces $P_{f_1}, P_{f_2}, ...P_{f_k}$, we get the vertex u and hence the original graph H.

The base case involves no interior vertices, we merge adjacent polygons around the shared interior edge. Using condition (ii) we get that new angles created in the interior are $\leq \pi$. So, the resulting convex polygon is just a simple convex polygon. We can easily recover the original graph from it. So, we just get the tessellation by a single convex polygon. □

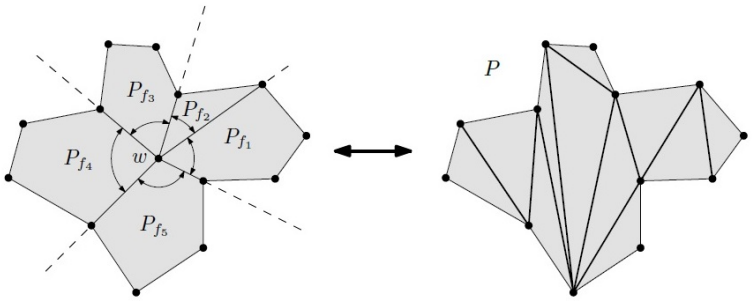

Figure 1.13: Triangulating the union of faces surrounding the vertex w, from [9]

Now that we have a lemma to ensure the existence of a tessellation, we can go back to our collection of radii, and hence kites,

We define H to be a subgraph of the primal-dual completion of G, i.e. $(G^{\diamond})^{\diamond}$. We have that $V_H = V/\{\xi, \xi'\} \bigcup F/\{\eta, \eta'\} \bigcup E/\{\xi\xi'\}$ and $E_H = \{(z, e), z \in V/\{\xi, \xi'\} \bigcup F/\{\eta, \eta'\}, e \in E/\{\xi\xi'\}\}$, with z incident to the edge $e \in E$ in G.

Claim H satisfies all the conditions of lemma 1.7.1.

Proof. Claim (i): H is 2-connected.

This follows from the 3-connectivity of G and G' that removal of one vertex cannot disconnect H, but there exists a set of three vertices whose removal would disconnect H.

Claim (ii): We have the edge lengths of the adjacent edges of the polygons associated with the inner edges.

This follows as a result of our iteration that the kites fit locally as they have the same edge length, dependent on the particular r_u and r_v.

Claim (iii) : $\sum_{f \in F_v} \beta_{f_v} = 2\pi$ for all the inner vertices.

As from the iteration, we have $\forall u \in U_{in}$, $\alpha_u(\hat{r}_u) = 2\pi$. As each edge of H involves 4 kites, every right angle of kite associated with an interior node is complemented by three other kites to form the angle sum 2π.

Claim (iv) : $\sum_{f \in F_v} \beta_{f_v} \leq \pi$.

The vertices of H which are incident to the outer face are either points where one or two right angles of kites meet, forming angle $\pi/2$ pr π, or they are nodes u in U_{in} which are adjacent to a vertex, say, w in U_o, as we defined earlier, the angle, in this case, is $\alpha uw = \pi$. As this angle is not part of H, the incident angles in H around u sum up to $\alpha_u(\hat{r}_u) - \alpha_{uw} = 2\pi - \pi = \pi$. So, the angle sums of the nodes incident to the outer face are either $\pi/2$ pr π. □

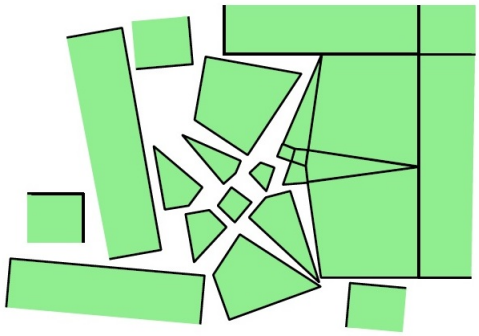

Figure 1.14: Laying out kites to obtaining the tessellation, from [9].

Since all the local matching conditions are met, now we can invoke Lemma 1.7.1, we get that all the bounded kites tessellate the plane and they are bounded in the rectangle R. The unbounded kites can be attached edge by edge onto the boundary of R.

1.8 Constructing the circle representation

Now that we have a layout for the kites, we wish to get the primal-dual circle representation from this layout. Since the kites naturally induce an overlaid straight line drawing of G and G' with only the outer face vertices missing,(they are all at ∞). For every primal-dual pair of edges, $xx' \in G$ and $yy' \in G'$, we have that the point of intersection (p) of these edges is right-angled in each of 4 involved kites so it would mean that the circles associated to these vertices touch tangentially at p.

For a node $u \in U_{in}$, consider all the kites containing u, as these kites can be put into cyclic order by rotation of $G^{\diamond}$ to form a polygon P_u and by the geometry of kites, we can see that P_u contains the circle C_u centered at u which touches P_u at the common points of the neighboring kites.

For $u \in \{\eta, \eta'\}$, the polygon P_u obtained by joining the unbounded kites is a half-plane, and line C_u goes through the right angle corners of the involved kites. Since polygons are pairwise distinct, we get that the circles corresponding to vertices of G and vertices of G' are pairwise disjoint.

Thus we have the collection $\{C_x\}$ and $\{D_y\}$ with all the proper tangency conditions to give the primal-dual circle representation. Once we have the primal-dual circle representations, we can go via inverse stereographic projections to obtain the primal-dual disk representation

of G on the sphere. This concludes the proof of theorem 1.3.3.

Chapter 2

Hyperbolic Geometry

In this chapter, we establish some definitions and results about hyperbolic geometry that will aid us in the study of hyperbolic knots and their complements. We have used [19], [3], [4], [12] and [2] as references.

2.1 Two dimensional Geometries

Around 300 BCE in his influential book "The Elements" Euclid formulated the foundations of geometry, now known as *Euclidean geometry*. Euclid gave 5 postulates about points, lines, circles, and angles. The last postulate known as the parallel postulate was the most interesting. Playfair in the late 18th century reformulated the parallel postulate as "given a line and a point outside the line, there exists a unique line passing through this point and parallel to the given line". For about 2000 years, mathematicians tried proving the fifth postulate using the first four postulates with little success. By the eighteenth century, mathematicians began studying geometries that satisfied the first four postulates but not the fifth. These geometries came to be known as *non-Euclidean geometries*. In two dimensions, the spherical and hyperbolic geometries are non-Euclidean.

In this chapter, we will discuss the hyperbolic plane $\mathbb{H}^2$ and the hyperbolic space $\mathbb{H}^3$, give models, describe geodesics and isometries.

2.2 The Hyperbolic plane

The upper-half plane model of the hyperbolic plane is $\mathbb{H}^2 = \{(x, y) \in \mathbb{R}^2 | y > 0\}$ with the metric,

$$ds^2 = \frac{dx^2 + dy^2}{y^2}$$

Note that $\mathbb{H}^2 = \{z \in \mathbb{C} |\ \mathrm{Im}(z) > 0\}$. The space inherits the notion of points and angles from $\mathbb{C}$.

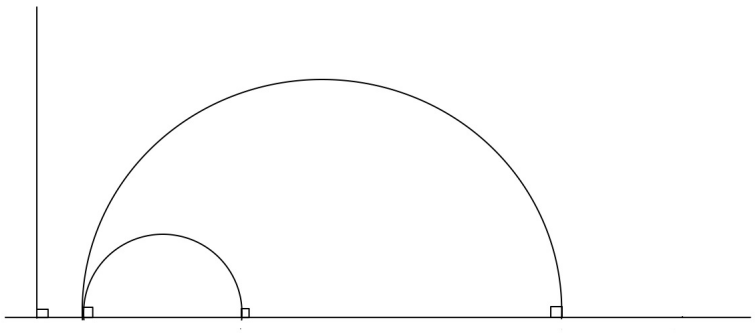

Figure 2.1: The geodesics in $\mathbb{H}^2$.

1. The hyperbolic length of a curve γ parameterized as $t \to (x(t), y(t))$ is given by,

$$l_{\mathbb{H}^2}(\gamma) = \int_a^b \frac{\sqrt{x'(t)^2 + y'(t)^2}dt}{y(t)}$$

2. The geodesics in $\mathbb{H}^2$ are Euclidean line and circles that meet the real axis $\mathbb{R}$ at right-angles. So the geodesics are vertical straight lines and semi-circles with centers on the real line. See Figure 2.1.

3. The *circle at infinity* of $\mathbb{H}^2$ is $\mathbb{R} \cup \infty$. This is also called the boundary $\partial\mathbb{H}^2$. Points on the circle at infinity are called *ideal points*.

4. A *horocycle* at an ideal point $p \in \partial\mathbb{H}^2$ is defined as a curve perpendicular to all the geodesics through p. If $p = \infty$, the horocycle is a horizontal line, else it is a circle tangent to the real axis. See Figure 2.2.

5. The region of $\mathbb{H}^2$ interior to a horocycle is known as the *horoball*.

6. An *ideal triangle* in $\mathbb{H}^2$ is a triangle with all three edges are geodesics and all the vertices on the boundary $\partial\mathbb{H}^2$.

2.2.1 Isometries of $\mathbb{H}^2$

We work with the upper half plane model of the hyperbolic 2-space. Since isometry preserves the metric, it preserves path lengths and areas.

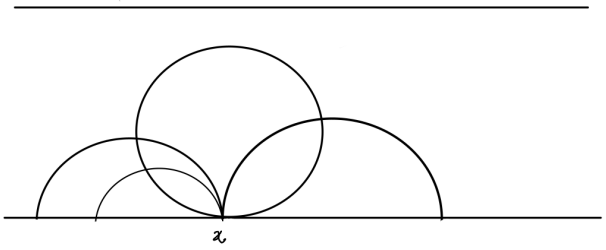

Figure 2.2: The horocycles centred at the pint x and the horizontal line.

It can be seen from the definition of the hyperbolic metric that the isometries of hyperbolic plane include horizontal translations $[(x, y) \to (x + x_0, y), x_0 \in \mathbb{R}]$, dilations $[(x, y) \to (\lambda x, \lambda y), \lambda > 0]$ and the reflection $(x, y) \to (-x, y)$. The standard inversions across the unit circle $\mathbb{S}^1$, given by $(x, y) \to (\frac{x}{x^2+y^2}, \frac{y}{x^2+y^2})$ is also a hyperbolic isometry, which can be expressed as a complex function $z \to \frac{1}{\bar{z}} = \rho^{-1}e^{i\theta}$.

The isometries obtained by composing dilations and horizontal translations immediately state that for every $P, Q \in \mathbb{H}^2$, there exists an isometry ϕ of $(\mathbb{H}^2, d_{\mathbb{H}^2})$, such that $\phi(P) = Q$, i.e. $\mathbb{H}^2$ is homogeneous.

All isometries of $\mathbb{H}^2$ are generated by the composition of the above-mentioned isometries. The group of isometries of $\mathbb{H}^2$ is generated by inversions in the upper half plane in hyperbolic geodesics. We classify all the isometries of hyperbolic 2-space using the following lemmas.

Lemma 2.2.1. *All maps of form* $z \to A(z) = \frac{az+b}{cz+d}$ *with* $a, b, c, d \in \mathbb{R}$ *such that* $ad-bc = 1$ *are isometries of* $(\mathbb{H}^2, d_{\mathbb{H}^2})$.

Proof. We wish to express the above transformation as a composition of the known isometries, namely, translations, reflections and inversions, rotations, and dilations. We look at two cases when $c = 0$ and when $c \neq 0$.

Case 1 c = 0;

$$A(z) = \frac{az+b}{cz+d} = \frac{c.(az+b)}{c.(cz+d)} = \frac{acz+bc+ad-ad}{c^2z+dc} = \frac{a(cz+d)+bc-ad}{c(cz+d)} = \frac{a}{c} + \frac{bc-ad}{c^2(z+\frac{d}{c})}.$$

Case 2 c = 0;

$$Az = \frac{a}{d}(z+\frac{b}{a})$$

In both cases, we can see that $A(z)$ can be written as a combination of the dilation, translation, and inversions, and hence is an isometry of $(\mathbb{H}^2, d_{\mathbb{H}^2})$. □

A similar result holds for the antilinear maps, i.e. $z \to B(z) = \frac{a\bar{z}+b}{c\bar{z}+d}$ with $a, b, c, d \in \mathbb{R}$ such that $ad - bc = 1$ by an identical argument. Now, conversely, we wish to show that the given any isometry of $\mathbb{H}^2$, it is of the form $A(z)$, for this we first see that,

Lemma 2.2.2. *Let ϕ be an isometry of $(\mathbb{H}^2, d_{\mathbb{H}^2})$, such that $\phi(iy) = iy \ \forall y > 0$. Then either $\phi(z) = z \ \forall z \in \mathbb{H}^2$ or $\phi(z) = -\bar{z} \ \forall z \in \mathbb{H}^2$.*

Proof. Let $L = \{iy : y > 0\}$ denote the upper half of y-axis. Thus, ϕ fixes L.
For every $iy \in L$, we denote by g_y a geodesic passing through iy orthogonal to L. Since ϕ is an isometry, therefore it sends g_y to a geodesic g passing through iy. We wish to show that $g = g_y$.
We use the property of geodesic that for any $y_1 > y$, the point iy is the point of g_y that is closest to iy_1. As ϕ is an isometry, $\phi(iy) = iy$ is the closest point of $\phi(g_y) = g$ that is closest to $\phi(iy_1) = iy_1$. Therefore, we get that $g = g_y$, and $\phi(g_y) = g_y$.
Now, we pick a point $P = a+ib$ on g_y, then its ϕ-image is one of the two points of g_y that are at a distance $d_{\mathbb{H}^2}(P, iy)$ from iy. One of these points is P itself and the other, by symmetry, is $-a+ib$. so, $\phi(a+ib) = a+ib$ or $-a+ib$ for every $a+ib \in \mathbb{H}^2$. in other words, $\phi(z) = z$ or $\phi(z) = -\bar{z}$, $\forall z \in \mathbb{H}^2$. □

Theorem 2.2.3. *The isometries of $(\mathbb{H}^2, d_{\mathbb{H}^2})$ are exactly the maps of the form,*

$$\phi(z) = \frac{az+b}{cz+d} \text{ with } a, b, c, d \in \mathbb{C} \text{ such that } ad - bc = 1$$

or

$$\phi(z) = \frac{a\bar{z}+b}{c\bar{z}+d} \text{ with } a, b, c, d \in \mathbb{C} \text{ such that } ad - bc = 1$$

Proof. As we proved in Lemma 2.2.1. we see that map of this form is an isometry of $\mathbb{H}^2$. Conversely, we let ϕ be any arbitrary isometry of $\mathbb{H}^2$ and once again let $L = \{iy : y > 0\}$ denote the upper half of the y-axis. As, we saw earlier that ϕ-image of L is a complete geodesic, i.e. a Euclidean semicircle bounded by two distinct points $u, v \in \mathbb{R} \cup \infty$. In addition to this, if we orient L from 0 to ∞, then without loss of generality we require the $\phi(L)$ is oriented from u to v. We consider two cases,

Case 1 when $u, v \neq \infty$. The hyperbolic isometry, $\psi(z) = \dfrac{az - au}{cz - cv}$ with $a, c \in \mathbb{R}$ chosen such that $ac(u - v) = 1$.

So, $\psi o \phi$ sends u to 0 and v to ∞. As it sends L to a complete geodesic and respects its orientation, therefore we can argue that there exists some $t > 0$ such that $\psi o \phi(t) = it$. Replacing $a \to a/\sqrt{t}$ and $c \to a/\sqrt{t}$, we get that $\phi o \psi(i) = i$. Therefore, $\psi o \phi$ sends each $iy \in L$ to a point of L that is at the same hyperbolic distance from i to iy, since orientation is preserved, we get that $\psi o \phi(iy) = iy$ for every $y > 0$.

By Lemma 2.2.2, we have that this composition is either z or $-\bar{z}$.

In the first case, $\psi o \phi(z) = z$, implies that $\phi(z) = \psi^{-1}(z) = \dfrac{-cvz + au}{-cz + a}$ upon solving.

The other case $\psi o \phi(z) = -\bar{z}$ implies that $\phi(z) = \psi^{-1}(-\bar{z}) = \dfrac{cvz + au}{c\bar{z} + a}$. Thus giving $\phi(z)$ of the desired form.

Case 1 For the case where either u or v is ∞, we can utilise the same argument for the isometries, $\psi(z) = \dfrac{-a}{cz - cv}$ when $ac = 1$ and $u = \infty$ and $\psi(z) = \dfrac{az - au}{c}$ when $ac = 1$ and $v = \infty$. □

So, we have established that all the orientation-preserving symmetries are of the fractional linear form, i.e Möbius transformations in dimension two.

$$z \to A(z) = \frac{az + b}{cz + d} \text{ with } a, b, c, d \in \mathbb{R} \text{ such that } ad - bc = 1 \tag{2.1}$$

They are conformal in nature and we can identify the groups of transformations with quotient $PSL(2, \mathbb{R}) := SL(2, \mathbb{R})/ \pm I$. We define the trace of a Möbius transformation as the trace of the normalized matrix of A, i.e. $\tau_A = trA = \pm(a + d)$.

Classification of the Möbius transformations of $\mathbb{H}^2$

Using the matrix form A $= \begin{bmatrix} a & b \\ c & d \end{bmatrix}$ for the isometry ϕ_A and trace τ_A we can classify the orientation preserving Möbius transformations, apart from identity by looking at the eigenvalues of A. The characteristic polynomial of A is given as,

$$\chi_A(\lambda) = \lambda^2 - \tau_A\lambda + 1$$

therefore the eigenvalues are $\dfrac{\tau_A \pm \sqrt{\tau_A^2 - 4}}{2}$, then we consider the following three cases,

1. $\tau_A = 2$, then eigenvalue is $\dfrac{\tau_A}{2}$, and ϕ_A is translation.

2. $\tau_A \in (-2, 2)$, then ϕ_A has a single fixed point, as $\tau_A^2 < 4$, the possible values of λ are conjugates and only one of them lies in $\mathbb{H}^2$. Thus, this is a hyperbolic rotation.

3. $\tau_A \in \mathbb{C}/[-2, 2]$, then A has two distinct eigenvalues since $\tau_A^2 > 4$, therefore ϕ_A is a dilation.

Cross Ratio

Given three distinct ideal points (p_2, p_3, p_4) none of them ∞, there exists a unique Möbius transformation, T, known that sends p_2 to 1, p_3 to 0 and p_4 to ∞, given by

$$T(z) = \frac{(z - p_3)(p_2 - p_4)}{(z - p_4)(p_2 - p_3)} = [z, p_2, p_3, p_4]$$

By definition $T(p_2) = 1, T(p_3) = 0$ and $T(p_4) = \infty$.

Given an ideal triangle Δ, there exists an isometry described above which takes Δ to an ideal triangle with vertices to 0, 1 and ∞. Thus all ideal triangles are isometric and have the same area.

2.3 Hyperbolic 3-space

We again consider the upper half space model,

$$\mathbb{H}^3 = \{(x_1, x_2, x_3) \in \mathbb{R}^3 | x_3 > 0\}$$

endowed with the hyperbolic metric $ds^2 = \dfrac{dx_1^2 + dx_2^2 + dx_3^2}{x_3^2}$.

1. The *sphere at infinity* is $\partial\mathbb{H}^3 = \mathbb{C} \cup \{\infty\}$.
2. As before, the geodesics of the hyperbolic 3-space are lines ad planes that are vertical and semicircles and hemispheres that meet the boundary $\partial\mathbb{H}^3$ at right angles.
3. A *horosphere* about ∞ in $\partial\mathbb{H}^3$ is a plane parallel to $\mathbb{C}$. A *horosphere* at a point $p \in \mathbb{C}$, is an Euclidean sphere tangent to $\mathbb{C}$ at p. A horoball is the region interior to a horosphere.
4. An ideal tetrahedron is a tetrahedron in $\mathbb{H}^3$ with all four vertices on $\partial\mathbb{H}^3$, and with geodesic edges and faces.

2.4 Isometries of $\mathbb{H}^3$

The usual isometries of $\mathbb{H}^3$ are extension of the isometries of $\mathbb{H}^2$, namely dilations, $(x_1, x_2, x_3) \to (\lambda x_1, \lambda x_2, \lambda x_3)$ for $\lambda > 0$; horizontal translations, $(x_1, x_2, x_3) \to (x_1 + a, x_2 + b, x_3)$ for $a, b \in \mathbb{R}$. We also have rotations about the x_3-axis, given as $(x_1, x_2, x_3) \to (x_1 cos\theta - x_2 sin\theta, x_1 sin\theta + x_2 cos\theta, x_3)$ for $\theta \in \mathbb{R}$. We also have inversions in the unit sphere $\mathbb{S}^2$, given by $(x_1, x_2, x_3) \to (\dfrac{x_1}{x_1^2 + x_2^2 + x_3^2}, \dfrac{x_2}{x_1^2 + x_2^2 + x_3^2}, \dfrac{x_3}{x_1^2 + x_2^2 + x_3^2})$.

Lemma 2.4.1. *Every linear (or antilinear) fractional map of $\hat{\mathbb{C}} = \mathbb{C} \cup \infty$ continuously extends to a map $\hat{\phi} : \mathbb{H}^3 \cup \hat{\mathbb{C}} \to \mathbb{H}^3 \cup \hat{\mathbb{C}}$, whose restriction to $\mathbb{H}^3$ is an isometry of $(\mathbb{H}^3, d_{\mathbb{H}^3})$.*

Proof. We recall Lemma 2.2.1 here, where we saw that a linear (or antilinear) fractional linear map $\phi : \hat{\mathbb{C}} \to \hat{\mathbb{C}}$ is a composition of translations, dilations and inversions. All these component functions can be extended to continuous transformations of $\mathbb{H}^3 \cup \hat{\mathbb{C}}$ inducing isometrics of $(\mathbb{H}^3, d_{\mathbb{H}^3})$. □

From the above lemma, it may be the case that the extension $\hat{\phi}$ of ϕ depends on the choice of decomposition of ϕ into translations, dilations or inversions. However, that is not the case, as we know that the inversion across the unit sphere sends any sphere S centered on the xy-plane to a sphere centered on the xy-plane, possibly a vertical plane since inversion is an isometry of $\mathbb{H}^2$. Then, given any point $p \in \mathbb{H}^3$, we can pick three spheres S_1, S_2, S_3 such that P is the only point of the intersection $\mathbb{H}^3 \cap S_1 \cap S_2 \cap S_3$. Using the usual isometries, the extension $\hat{\phi}$ sends S_i to S_i' for all i, and hence p to $\phi(p)$ as, $\phi(p)$ is the unique intersection of $\mathbb{H}^3 \cap S_1' \cap S_2' \cap S_3'$, and therefore we have that,

Lemma 2.4.2. *The extension $\hat{\phi} : \mathbb{H}^3 \to \mathbb{H}^3$ of a linear(or antilinear) map $\phi : \hat{\mathbb{C}} \to \hat{\mathbb{C}}$ is independent of choices.*

Theorem 2.4.3. *Every linear (or antilinear) fractional map $\phi : \hat{\mathbb{C}} \to \hat{\mathbb{C}}$ has a unique continuous extension $\hat{\phi} : \mathbb{H}^3 \cup \hat{\mathbb{C}} \to \mathbb{H}^3 \cup \hat{\mathbb{C}}$, whose restriction to $\mathbb{H}^3$ is an isometry of $(\mathbb{H}^3, d_{\mathbb{H}^3})$.*
Conversely, every isometry of $(\mathbb{H}^3, d_{\mathbb{H}^3})$ is obtained this way.

Proof. We have the existence from Lemma 2.4.1. Let ψ denote an isometry of $(\mathbb{H}^3, d_{\mathbb{H}^3})$. Now, we wish to find a linear(or antilinear) map ϕ whose isometric extension to $\mathbb{H}^3$ agrees with ψ.
Being an isometry ψ sends the oriented geodesic 0∞ to another complete geodesic of $\mathbb{H}^2$ oriented from $z_1 \to z_2$, as there is a linear fractional transformation taking $0 \to z_1$ and $\infty \to z_2$, therefore, $\psi o \phi^{-1}$ sends the geodesic to itself. Without loss of generality, we replace $\psi o \phi^{-1}$ with ψ.
Composing with scaling, we get that ψ fixes some and hence all points of 0∞. Let g be a complete geodesic in the half plane $\mathbb{H}^2 \subset \mathbb{H}^3$ and crosses 0∞ at a point P_0. The, $\psi(g)$ is a complete geodesic passing through P_0. As $\mathbb{H}^2$ may be realized as a union of complete geodesics that meet both 0∞ and $g - \{P_0\}$. Therefore, $\psi(\mathbb{H}^2)$ is the union of complete geodesics that meet both 0∞ and $\psi(g) - \{\psi(P_0)\}$. Composing with an isometry, if necessary, we get that $\psi(\mathbb{H}^2) = \mathbb{H}^2$.
Thus, ψ restricts to an isometry on $\mathbb{H}^2$. Now, by theorem 2.2.3, we find a linear(or antilinear) fractional map ϕ, with real coefficients such that $\hat{\phi}$ coincides with ψ. Then $\psi o \phi^{-1}$ is a hyperbolic isometry of $\mathbb{H}^3$, which fixes every point. We argue as in Lemma 2.2.2 that $\psi o \phi^{-1}$ is either identity or euclidean reflection across $\mathbb{H}^2$. Lemma 2.4.2 gives the uniqueness of this extension $\hat{\phi}$. □

Hence, we see that the group of orientation-preserving isometries of $\mathbb{H}^3$ is $PSL(2,\mathbb{C}) = SL(2,\mathbb{C})/\pm I$. It acts on the boundary $\partial\mathbb{H}^3$ via Möbius transformations.
sing the matrix form $\begin{bmatrix} a & b \\ c & d \end{bmatrix}$ and trace τ_A we can classify the orientation preserving Möbius transformations, apart from identity as,

1. **Parabolic** A is parabolic if the following equivalent criteria is satisfied:

   - A is conjugate to $z \to z + 1$.
   - A has exactly one fixed point in $\mathbb{S}^2$.
   - $\tau_A = \pm 2$ and $A \neq id$.

2. **Elliptic** A is elliptic if the following equivalent criteria is satisfied:

   - A is conjugate to $z \to e^{2i\theta}z$, with $2\theta \neq 2\pi$.
   - A has two fixed points in $\mathbb{S}^2$ and the derivative of A has absolute value 1 at both of them.
   - $\tau_A \in (-2, 2)$.

3. **Loxodromic** A is loxodromic if the following equivalent criteria are satisfied:

   - A is conjugate to $z \to \lambda^2 z$ with $|\lambda| > 1$.
   - A has two fixed points in $\mathbb{S}^2$, one with $|A'| < 1$, attracting and one with $|A'| > 1$, repelling.
   - $\tau_A \in \mathbb{C}/[-2, 2]$.

A detailed proof for the above classification can be found in [12].

As discussed in the following section, given four ideal vertices of a given ideal tetrahedron, there exists a Möbius transformation taking them to 0,1,∞ and z. The number z characterizes the ideal tetrahedron up to isometry and is called the *cross ratio parameter* of the ideal tetrahedron.

2.4.1 Poincaré Disk Model

The underlying space for this model is the Euclidean unit disk in n dimensions $\mathbb{D}^n$,
$\mathbb{D}^n = \{\vec{x} \in \mathbb{R}^n : ||x|| < 1\}$, with the metric $ds^2 = \dfrac{4||d\vec{x}||^2}{(1-||\vec{x}||^2)^2}$.
This model is conformal in nature. The geodesics are Euclidean circles meeting $\partial\mathbb{D}^n$ at right angles or intersection of Euclidean lines through the origin with $\mathbb{D}^n$.
We have discussed here two planar models for the hyperbolic space, namely the upper half space model and the Poincaré disk model. There are several non-planar models of hyperbolic space as well, for example the hyperboloid model and the Klein model. A detailed description of these can be found in [3]. We have isometries of the hyperbolic space $\mathbb{H}^n$ taking one model to the other. For example, the upper half space model and the Poincaré disk model are related by the differentiable mapping,

$$i : \mathbb{D}^n \to \mathbb{R}^n \text{ as } x \mapsto 2\frac{x+e_n}{||x+e_n||^2} - e_n$$

where $e_n = (0, 0, ..., 1)$ and $||.||$ denotes the Euclidean norm on $\mathbb{R}^n$.

2.5 Isometries of $\mathbb{H}^n$

Let $\mathcal{I}(\mathcal{M})$ for a Riemannian manifold $\mathcal{M}$ denote the sets of all isometric diffeomorphisms of $\mathcal{M}$ onto itself. If $\mathcal{M}$ has an orientation, we denote the set of all orientation-preserving isometries of $\mathcal{M}$ as $\mathcal{I}^+(\mathcal{M})$. Both the sets form groups under composition.
We denote the set of conformal diffeomorphisms of $\mathcal{M}$ onto $\mathcal{N}$ by $Conf(\mathcal{M}, \mathcal{N})$, so $Conf(\mathcal{M})$ and $Conf^+(\mathcal{M})$ denote the set of all conformal diffeomorphisms of $\mathcal{M}$ onto itself and the orientation preserving self-diffeomorphisms of $\mathcal{M}$ respectively. Again, both of these sets form groups under composition. Having studied the inversions with respect to $\mathbb{S}^1, \mathbb{S}^2$, we now define inversions in a more general setting, as

Definition 2.5.1. *If $x_0 \in \mathbb{R}^n$ and $\alpha > 0$, the inversion with respect to the sphere $M(x_0, \alpha)$ with centre x_0 and radius $\sqrt{\alpha}$, is defined as the following mapping:*

$$i_{x_0,\alpha} : x \mapsto \alpha.\frac{x-x_0}{||x-x_0||^2} + x_0$$

We deduce that inversion $i_{x_0,\alpha}$ is a conformal mapping.

Lemma 2.5.1. *For the manifold $\mathbb{D}^n$, unit ball endowed with the metric described above, we have that, the isometries of $\mathbb{D}^n$ are precisely the conformal mappings of open Euclidean unit ball D^n of $\mathbb{R}^n$.*

Theorem 2.5.2.

$$\mathcal{I}(\mathbb{H}^n) = Conf(\mathbb{H}^n) \text{ and } \mathcal{I}^+(\mathbb{H}^n) = Conf^+(\mathbb{H}^n)$$

Proof. Consider the diffeomorphism

$$i : \mathbb{D}^n \to \mathbb{R}^n \text{ as } x \mapsto 2\frac{x + e_n}{||x + e_n||^2} - e_n$$

where $e_n = (0, 0, ..., 1)$ and $||.||$ denotes the Euclidean norm on $\mathbb{R}^n$. We can see that this is the inversion with respect to center $(0, 0, ...0, -1)$ and radius $\sqrt{2}$. Hence, this map is conformal. Using the lemma 2.5.1, we see that the isometries of $\mathbb{H}^n$ are the conformal mappings of $\mathbb{H}^n$. □

Chapter 3

Hyperbolic knots and links

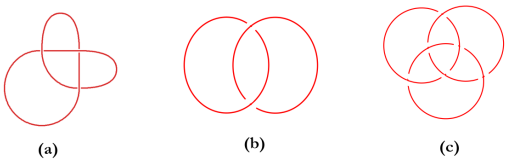

Figure 3.1: (a) Trefoil Knot; (b) Hopf Link; (C) Borromean Rings

In this chapter, we discuss knots and links whose complements admit hyperbolic structure. We have based the content of this chapter on material from [16].

3.1 Terminology

Definition 3.1.1. *A knot $K \subset S^3$ is a subset of points homeomorphic to S^1 under a piecewise linear(PL) homeomorphism. Alternatively, we can think of a knot as a PL embedding $K : S^1 \to S^3$.*

Examples: See Figure 3.1 (a) the parametrization, $x = sint + 2sint2t$, $y = cost - 2cos2t$, $z = -sin3t$, gives the *trefoil* knot.

Definition 3.1.2. *A link is a subset of S^3 PL-homeomorphic to a disjoint union of copies of S^1, alternatively a PL-embedding of disjoint copies of S^1 into S^3.*

Examples: See Figure 3.1 Borromean rings, the Hopf link.

Definition 3.1.3. *We say that two knots K_1, K_2 are said to be equivalent if they are ambient isotopic, i.e $\exists$ a PL-homotopy $h : S^3 \times [0,1] \mapsto S^3$ such that $h(*,t) = h_t : S^3 \mapsto S^3$ is a homeomorphism for each t, and $h(K_1, 0) = h_0(K_1) = K_1$ and $h(K_1, 1) = h_1(K_1) = K_2$.*

Remark

1. We generally use the symbol K for both the embedding and image $K(S^1)$.
2. We will also use smooth embeddings, diffeomorphisms, and smooth homotopies/isotopies instead of PL homeomorphisms. In dimension 3, since the PL and smooth categories are equivalent [14], we can switch between the two categories.

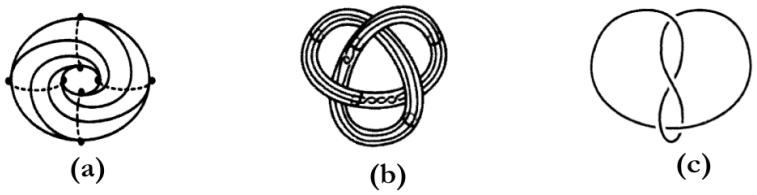

Figure 3.2: (a) A Torus knot, *trefoil*; (b) a satellite knot, *a second whitehead double of the trefoil*; (c) a hyperbolic knot, *the Figure-8 knot*, from [1]

3. An embedding of S^1 into S^3 that can not be made piecewise linear defines a *wild knot*. We avoid wild knots in our discussions, as doing so will enable us to assume that a knot has a regular tubular neighborhood, i.e. there is an embedding of $S^1 \times D^2$ in S^3 such that $S^1 \times \{0\}$ maps to the knot.

Definition 3.1.4. *A torus knot is a knot that can be embedded on the surface of an unknotted torus in S^3. See Figure 3.2 (a).*

Example: The trefoil knot is the (3,2) torus knot, where 3 denotes the number of times the knot wraps meridionally around the torus and 2 denotes that the knot wraps twice longitudinally around the torus.

Definition 3.1.5. *A satellite knot is a knot that can be embedded in a regular neighborhood of another knot in S^3. See Figure 3.2 (b).*

Definition 3.1.6. *(i)For a knot K, let $N(K)$ denote an open regular neighbourhood of K in S^3; (ii) The knot exterior is defined to be the manifold, $S^3/N(K)$; (iii) The knot complement is the open manifold S^3/K, homeomorphic to the interior of $S^3/N(K)$.*

Definition 3.1.7. *A knot or link L is said to be hyperbolic if the manifold S^3/L can be given a metric of constant curvature -1. See Figure 3.2 (c).*

Thurston showed that a knot complement will either be Seifert-fibered, toroidal or hyperbolic.

Theorem 3.1.1. *(Thurston [21]) The knots whose complement can be Seifert-fibered consist of torus knots. Toroidal knot complements are exactly the satellite knots. All other knots are hyperbolic.*

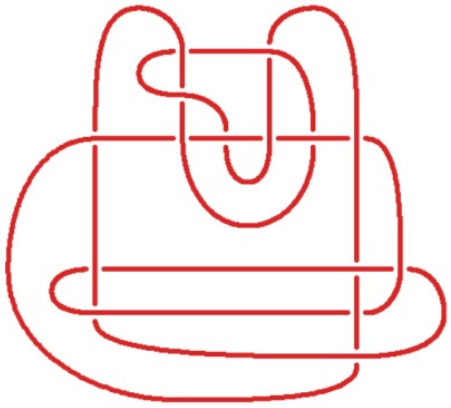

Figure 3.3: A projection of the link $K15a58938$, from [7]

Hyperbolic knots form the largest class of knots, we discuss the decomposition of hyperbolic knot complements in detail in the sections to follow. By the Mostow-Prasad rigidity theorem, stated later, we have that if a knot complement admits a hyperbolic structure then that structure is unique. Since the decomposition of the complements of the alternating knot follows the combinatorics of the link diagram, and hence the hyperbolic geometry of the alternating knot complements may be understood via the knot diagrams.

3.2 Link diagrams

Definition 3.2.1. *A knot(or link) diagram is a 4-valent graph with over/under crossing information at each vertex. The diagram is embedded in a plane $S^2 \subset S^3$, called the projection plane.*

Example: Figure 3.3 depicts a projection of the knot $K15a58938$.

Definition 3.2.2. *A projection graph $\Gamma(L)$ of link (L) refers to a 4-valent graph of a link when projected in a plane. The regions of the plane cut by the projection graph are called faces of $\Gamma(L)$.*

Definition 3.2.3. *An alternating diagram of a knot is a diagram with an orientation which when followed the strand goes through over and under crossings alternatively. An alternating knot or link is a knot or link that has an alternating diagram.*

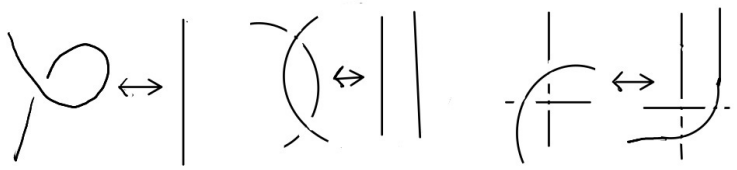

Figure 3.4: The three Reidemeister moves

Figure 3.5: (a) A nugatory crossing; (b) A reducible crossing

There are some properties of the knot diagrams which serve as knot invariants. For example, there are loops that can be untwisted to simplify the knot diagram, and the three Reidemeister moves, Figure 3.4 to change the knot diagram equivalently into another diagram.

Definition 3.2.4. *A nugatory crossing is a single crossing forming a loop, as shown in Figure 3.5 (a). A reducible crossing, Figure 3.5 (b) is a crossing through which we may draw a circle γ on the plane of projection such that γ meets the diagram only at one point. A knot diagram is said to be reduced if it contains no reducible crossings.*

Definition 3.2.5. *A twist region is a string of bigon regions in a knot diagram arranged end-to-end from one end to the other.*

Definition 3.2.6. *For any twist region of any link diagram, we add an unknotted component to the diagram which encircles the two strands of the link. The resulting link is said to be augmented, the added link component, an unknotted component is called a crossing circle and the original link components are called knot strands.*

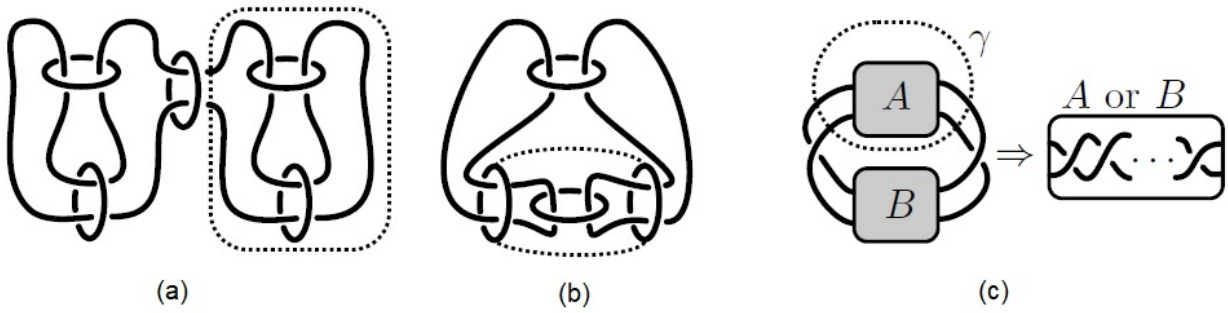

Figure 3.6: (a) A fully augmented link with a diagram that is not prime; (b) A fully augmented link that is not reduced; (c) The diagram is twist-reduced if one of the regions A or B consists of only of bigons in a twist region.

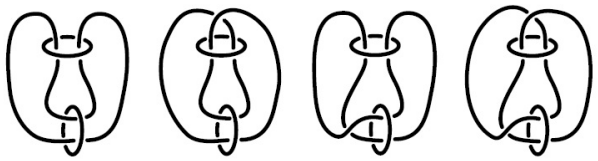

Figure 3.7: Some fully augmented links from [16]

When a crossing circle is added to all twist regions in a knot diagram, the resulting link is said to be fully augmented.

Example: Figure 3.6 and 3.7 depict some fully augmented links.

Fully augmented links form a special subclass of links with interesting geometric properties [15]. The hyperbolic volume of fully augmented link complements come up in our volume computations in Chapter 6.

Definition 3.2.7. *A fully augmented link with a link diagram L is called reduced if the following hold.*

1. *L is connected.*
2. *L is prime, i.e. any closed curve meeting the diagram twice bounds a region on one side with no crossings.*
3. *None of its crossing circles are parallel. That is, there are no closed curves in the diagram running over exactly two crossing circles and meeting exactly two white faces*

on either side of the two crossing circles.

Definition 3.2.8. *A diagram is twist-reduced if it bounds a string of bigons arranged end-to-end in a simple closed curve that meets the diagram exactly twice in two crossings.*

3.3 Determining the geometry of the knot complement

In this section, we begin by discussing the decomposition of manifolds into topological ideal polyhedra and then we study the hyperbolic structures on manifolds.

Definition 3.3.1. *1) Let M be a 2-manifold. A topological polygonal decomposition of M is a combinatorial way of gluing polygons so that the result is homeomorphic to M.*
2) A geometric polygonal decomposition of M is a topological polygonal decomposition along with a metric on each polygon such that gluing is by isometry and the result of the gluing is a smooth manifold with a complete metric. [16]

Definition 3.3.2. *Let X be a manifold, and G a group acting on X. We say that a manifold M has a (G,X)-structure if for every point $x \in M$, there exists a chart (U, ϕ),where $U \subset M$ and $\phi(U) \subset M$ open, and if two charts (U, ϕ) and (V, ψ) overlap, then the transition map $\gamma = \phi o \psi^{-1} : \psi(U \cap V) \to \phi(U \cap V)$ is an element of G.*

Example (1): Consider the Euclidean torus $T^2 = \mathbb{R}^2/\mathbb{Z}^2$, let X be the two dimensional euclidean space $\mathbb{R}^2$ and $G = \text{Isom}(\mathbb{R}^2)$.Then, T^2 admits a $(\text{Isom}(\mathbb{R}^2), \mathbb{R}^2)$-structure as follows, let $p : \mathbb{R}^2 \to T^2$ be a covering map. Pick a point $p \in T^2$, let V be the open disc around p, and $U \subset \mathbb{R}^2$ be such that $p|_U : U \to V$ is a homeomorphism. Then, $((D, p|_U^{-1}))$ is a chart around p. If two charts $(U, p|_U^{-1})$ and $(V, p|_V^{-1})$ overlap, then the transition map $\gamma = (p|_U^{-1}) o (p|_V^{-1})^{-1}$ is a euclidean translation.

Definition 3.3.3. *Let $X = \mathbb{H}^2$ and G be Isom($\mathbb{H}^2$). We say that a 2-manifold N is hyperbolic or admits a hyperbolic structure when N has a $(Isom(\mathbb{H}^2), \mathbb{H}^2)$-structure.*

We may obtain hyperbolic manifolds of dimension two from geometric polygonal decomposition. We begin with a collection of hyperbolic polygons in $\mathbb{H}^2$,(say triangles) such that each polygon is convex and edges of the polygons are portions of geodesic curves in $\mathbb{H}^2$. To each edge, we associate one other edge and glue the polygons along the associated edge. This

gluing admits a hyperbolic structure if every point has a neighborhood that is isometric to a disc in the hyperbolic plane. Furthermore, we have that gluing hyperbolic polygons gives a manifold with hyperbolic structure if and only if the angle at each vertex of the polygons sums up to 2π.
Moving onto the discussion on the completeness of the metric, we define the concept of developing map and holonomy.

Developing map and holonomy

Consider a manifold M with a (G, X)-structure, where G is the group of real analytic diffeomorphisms acting transitively on X. Consider the universal cover $\tilde{M}$ of M, and consider an element $[\alpha] \in \tilde{M}$, where $\alpha : [0,1] \to M$ is the representative path of the class $[\alpha]$, we fix a base point $\alpha(0) = x_0 \in M$ contained in the chart (U_0, ϕ).
Now we find a partition $0 = t_0 < t_1 < t_2..... < t_n = 1$ for the charts (U_i, ϕ_i) such that $\alpha([t_i, t_{i+1}]) \subset U_i \ \forall i$. Denote the points $\alpha(t_i)$ as x_i. Therefore, each $x_i \in U_{i-1} \cap U_i$ for all i. Then the transition map $\gamma_{i-1,i} = \phi_{i-1} o \phi_i$ acting on x_i is a well defined element in G. We first extend ϕ_0 to $\Phi_1(t) : [0, t_2] \to X$ as,

$$\Phi_1(t) = \begin{cases} \phi_0(\alpha(t)) & \text{if } t \in [0, t_1] \\ \gamma_{0,1}(x_1).\phi_1(\alpha(t)) & \text{if } t \in [t_1, t_2] \end{cases}$$

As, $\phi_0(\alpha(t_1)) = \gamma_{0,1}(x_1).\phi_1(\alpha(t_1))$, this map is well defined in $[0, t_2]$. Now we inductively extend this map to $\Phi_i(t) : [0, t_{i+1}] \to X$ as,

$$\Phi_i(t) = \begin{cases} \Phi_{i-1}(t) & \text{if } t \in [0, t_i] \\ \gamma_{0,1}(x_1).\gamma_{1,2}(x_2).....\gamma_{i-1,i}(x_i).\phi_i(\alpha(t)) & \text{if } t \in [t_i, t_{i+1}] \end{cases}$$

Again as $\Phi_{i-1}(\alpha(t_i)) = \gamma_{0,1}(x_1).\gamma_{1,2}(x_2).....\gamma_{i-2,i-1}(x_{i-1}).\phi_{i-1}(\alpha(t))$ and as $\phi_{i-1}(\alpha(t_i)) = \gamma_{i-1,i}.\phi_i(\alpha(t_i))$, this map is well-defined. We repeat the process $n-1$ times and end up with $\Phi_{n-1} : [0,1] \to X$.

Definition 3.3.4. *The developing map $D : \tilde{M} \to X$ is the map $D([\alpha]) = \Phi_n(1) = \gamma_{0,1}(x_1).\gamma_{1,2}(x_2).....\gamma_{(n-2),(n-1)}(x_{n-1}).\phi_{n-1}(\alpha(1))$.*

From this construction, we also get a map $\Phi_{[\alpha]} : U \to X$, where U is a neighbourhood of

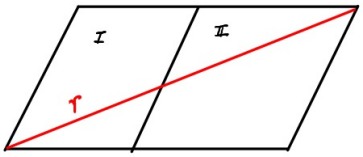

Figure 3.8: Developing a Euclidean torus

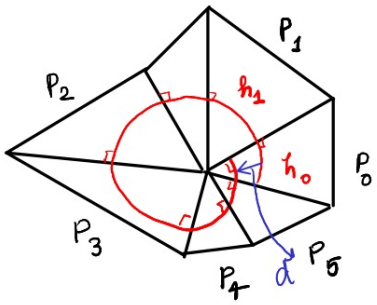

Figure 3.9: Extending a horocyle inside the manifold

$\alpha(1)$, as,

$$\Phi_{[\alpha]}(x) = \gamma_{0,1}(x_1).\gamma_{1,2}(x_2).....\gamma_{(n-2),(n-1)}(x_{n-1}).\phi_{n-1}(x)$$

Now, if $[\alpha] \in \tilde{M}$ is a homotopy class of loops based at x_o in M. Then, $(U, \Phi_{[\alpha]})$ and (U_0, ϕ_0) are two charts in the neighbourhood of x_0, they differ by an element of G, say $g_{[\alpha]}$, such that $\Phi_{[\alpha]} = g_{[\alpha]}.\phi_0$. Using the covering transformations of $\tilde{M}$, we can show that,

Lemma 3.3.1. *The map $\rho : \pi_1(M, x_0) \to G$ given as $[\alpha] \mapsto g_{[\alpha]}$ is a group homomorphism.*

Definition 3.3.5. *The element $g_{[\alpha]}$ is called the holonomy of $[\alpha]$. The group homomorphism ρ is called the holonomy of M. Its image, $\rho(\pi_1(M, x_0))$ is the holonomy group of M.*

Example: We consider the Euclidean torus. Pick a meridional and longitudinal curve on the torus and let x bet the intersection point of the two. Now, we consider a non-trivial curve γ based at x. The point x has a chart mapping x onto the Euclidean plane, let it be a parallelogram (I) with the usual gluing to get a torus. As the curve γ (in red) passes through the meridian (or longitude), we must glue the next parallelogram (II) opposite to the side we left. See Figure 3.8. We continue the process resulting in a tiling of the plane by the parallelograms which is the image of the developing map, or it is the developing image of the Euclidean torus.

3.3.1 Completion of polygonal gluings

Let M be an oriented hyperbolic 2-manifold obtained by gluing ideal hyperbolic polygons. An ideal vertex of M is an equivalence class of the ideal vertices of the polygons, identified via gluing. Let v be an ideal vertex of M, then v is identified with some vertex v_0 of a polygon P_0, let h_0 be the horocycle centered at v_0 on P_0. h_0 meets an edge e_0 of P_0 such that a polygon P_1 is glued through the edge e_0, meeting an ideal vertex v_1, which is identified to v. Hence, h_0 can be extended to a h_1, a horocycle centered at v_1. We continue the process counter-clockwise, and since we have a finite number of polygons, we end up again at vertex v_0 of P_0. See Figure 3.9.

Definition 3.3.6. *Let d(v) denote the signed distance, marked by a blue arrow in Figure 3.9, between h_0 and h_1 on P_0. The sign is taken such that if h_n is closer to v_0 than h_0, then it is positive.*

Note that $d(v)$ does not depend on the choice of h_0 and v_0. The computation of $d(v)$ can be done easily if we look at the polygons in $\mathbb{H}^2$ using developing maps and holonomy as follows:
We begin by fixing a vertex $v_0 \in P_0$, then we put P_0 in $\mathbb{H}^2$ with v_0 at ∞. We then take a horocycle h_0 centered at ∞ intersected with P_0. We follow h_0 to the right and where it meets the edge of P_0, P_1 is glued, the developing map aids us in embedding P_2 in $\mathbb{H}^2$. We continue the horocycle until it meets the vertex v_0 at ∞. When this happens we will glue an isometric copy of polygon P_0 to the P_0 we started with, with isometry (say, f) being the holonomy of the closed path encircling ideal vertex v counter-clockwise, taking h_0 to $f(h_0)$, which is at a distance $d(v)$ from the extended horocycle h_0. See Figure 3.10. Hence we are in the position to state the following theorem,

Theorem 3.3.2. *Let S be a surface with a hyperbolic structure obtained by gluing hyperbolic polygons. Then, the metric on S is complete if and only if $d(v) = 0$ for all ideal vertices v.*

Using the concept of developing maps and holonomy, Thurston proved the following criterion for completeness that holds in all dimensions and all geometries:

Theorem 3.3.3. *Let M be an n-manifold with a (G,X)-structure, where G acts transitively on X, and X admits a completely G-invariant metric. Then, the metric on M inherited from X is complete if and only if the developing map $D : \tilde{M} \to X$ is a covering map. [22]*

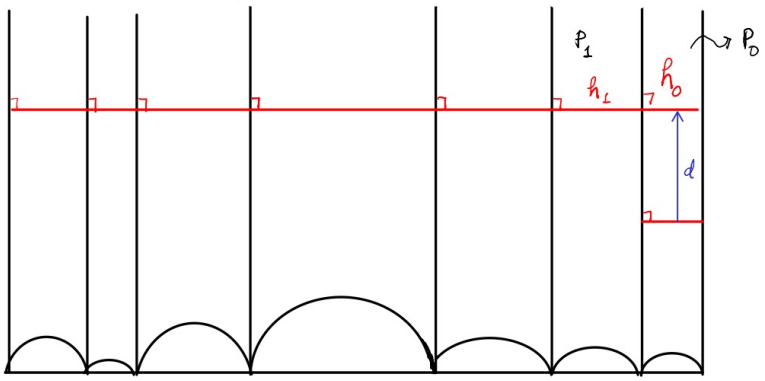

Figure 3.10: Extending the horocycle in $\mathbb{H}^2$

3.3.2 Polyhedral Decomposition of alternating link complement

Here we discuss the polyhedral decomposition of a knot (K) complement. We decompose $S^3 - K$ into two ideal polyhedra. These polyhedra can be realized as two balloons: one expanding above the diagram and one below the diagram. The balloons meet in the regions cut out by the diagram of the knot. We label these regions of the diagram, they will correspond to the faces of the polyhedra. The faces meet up at the edges, there is one edge for each crossing, and the edge runs vertically from the top of the crossing to the bottom. We give a step-by-step construction for a combinatorial method to describe the polyhedra.

Step 1 We start by labeling the regions of the projection plane cut by the graph of the knot. We put edges at each crossing to connect the two arcs, these arcs are known as the *crossing arcs*. We draw each edge four times, with the edge being ambient isotopic to the other three.

Step 2 Now we shrink the knot to the ideal vertices on the top polyhedra. While talking about the top polyhedron, we see that two of the edges of the over-strand are isotopic and we may identify them. Now we shrink each over-strand to ideal vertices. The resulting picture consists of a pattern of faces, edges and vertices in a view of the top polyhedron.

Step 3 We do the same construction, but for the bottom polyhedra. We first identify the two isotopic edges on the under-strand and then collapse each under-strand to the ideal

vertices. The resulting pattern depicts the bottom polyhedron viewed from the outside.

Polyhedral Decomposition of Figure-8 complement

We consider the example of the complement of the Figure-8 knot. We follow the steps 1-3 described in Figure 3.11. We label the regions of the projection graph, see Figure 3.11 (a), and we put four ambient isotopic edges from an over-strand to an under-strand, Figure 3.11 (b). We then construct the top polyhedron viewed from inside by identifying isotopic edges, Figure 3.11 (c), and shrink knot strands to the ideal vertices, Figure 3.11 (d). We do a similar process for the bottom polyhedron viewed from outside, see Figure 3.11 (e), (f).

Now that we have both the top and the bottom polyhedra, we glue them face-wise. Note that we have to glue them via a clockwise rotation to respect the orientations for each face labeled in the knot diagram in Figure 3.11 (a). Hence, we have obtained a polyhedral decomposition for the complement of the Figure-8 knot.

The polyhedra obtained above may contain bigons, a face with two edges and two ideal vertices. Since both edges are isotopic due to each face being simply connected, we may collapse the bigon to a single edge. In our case, the bigons between $(u_1, u_2), (u_3, u_4)$ and $(v_1, v_2), (v_3, v_4)$ may be collapsed and we get the result for top polyhedron, Figure 3.12 (a) and the bottom polyhedron, Figure 3.12 (b). We get that each polyhedron is in fact a tetrahedron.

Polyhedral Decomposition of Borromean rings complement

Here we discuss the polyhedral decomposition of the complement of the Borromean rings. One distinguishing feature here is that the knot diagram has no bigons. Figure 3.13 (a) through (f) depict the step-by-step application of the algorithm described above to get the top polyhedron viewed from inside, Figure 3.13 (d) and bottom polyhedron viewed from outside, Figure 3.13 (f).

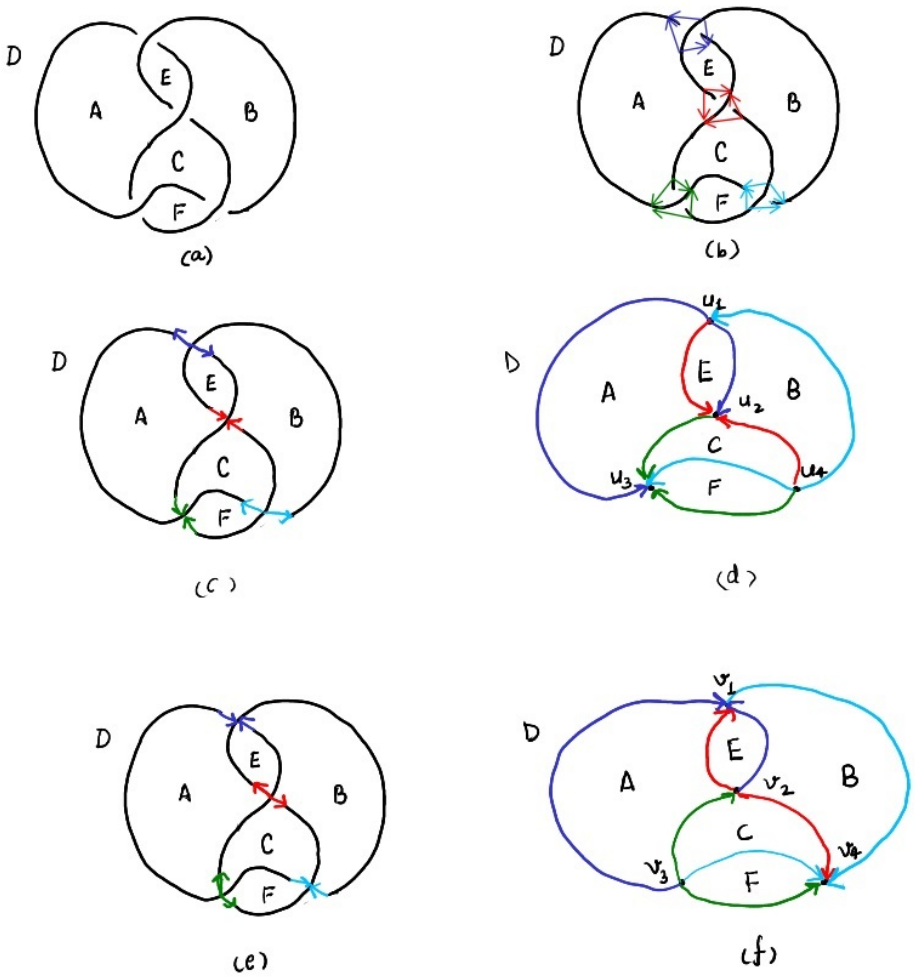

Figure 3.11: Polyhedral decomposition of the knot 4_1 into top and bottom polyhedra.

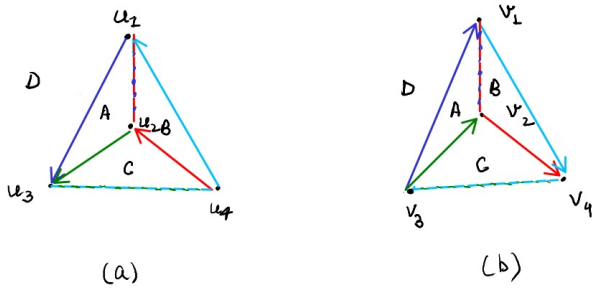

Figure 3.12: (a) Top and (b) Bottom, polyhedra with bigons removed.

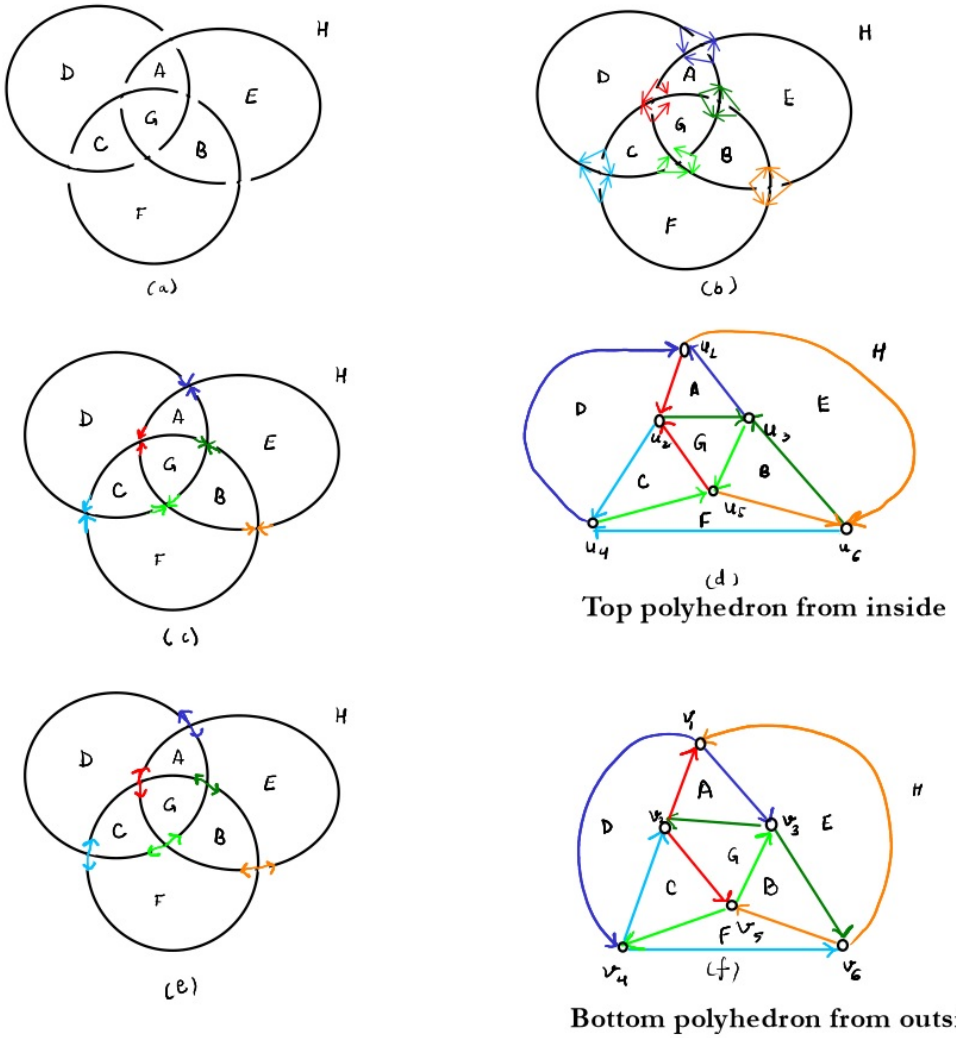

Figure 3.13: Polyhedral Decomposition of the link *L6a4* into top and bottom polyhedra.

3.4 Hyperbolic Structures: Triangulations and Gluing

Now we move on to study the polyhedral decomposition in three dimensions and in particular decomposition into ideal tetrahedra.

Definition 3.4.1. *Let M be a 3-manifold. A topological ideal triangulation of M is a combinatorial way of gluing truncated tetrahedra (ideal tetrahedra) so that the result is homeomorphic to M. Truncated parts will correspond to the boundary of M.*

For any given knot complement, we take its polyhedral decomposition, as defined in the earlier section and for each face, we pick an ideal vertex and subdivide the face into triangles sharing the chosen ideal vertex. Now, if we glue the polyhedra, keeping in mind the chosen vertex at each face, it results in a topological ideal triangulation for the complement of the knot.

Example 2 continued: Triangulation of the polyhedra associated to the Borromean rings

We begin with the polyhedra obtained in Figure 3.13. Earlier, we were viewing the top polyhedra from the inside, we now reflect it and rotate to get Figure 3.14 (a). To understand triangulation better, we map out faces and vertices on a regular octahedron, see Figure 3.14 (b). We put an edge between the vertices u_3, u_4, dashed black line in Figure 3.14 (a), and we get four tetrahedra as shown in Figure 3.14 (c). We do the same process for the bottom polyhedron, visualized in Figure 3.13, and we join the vertices v_3, v_4, see Figure 3.14). The bottom polyhedra divides into four tetrahedra depicted in Figure 3.14 (f). This gives a topological ideal triangulation for the complement of Borromean rings. All four tetrahedra are glued face-wise following the direction of the edges.

Edge parameters for ideal tetrahedra

Let T be an ideal tetrahedron embedded in $\mathbb{H}^3$, it has six edges. Suppose we pick and edge and send its endpoints to 0 and ∞, then via a unique möbius transformation (an isometry)

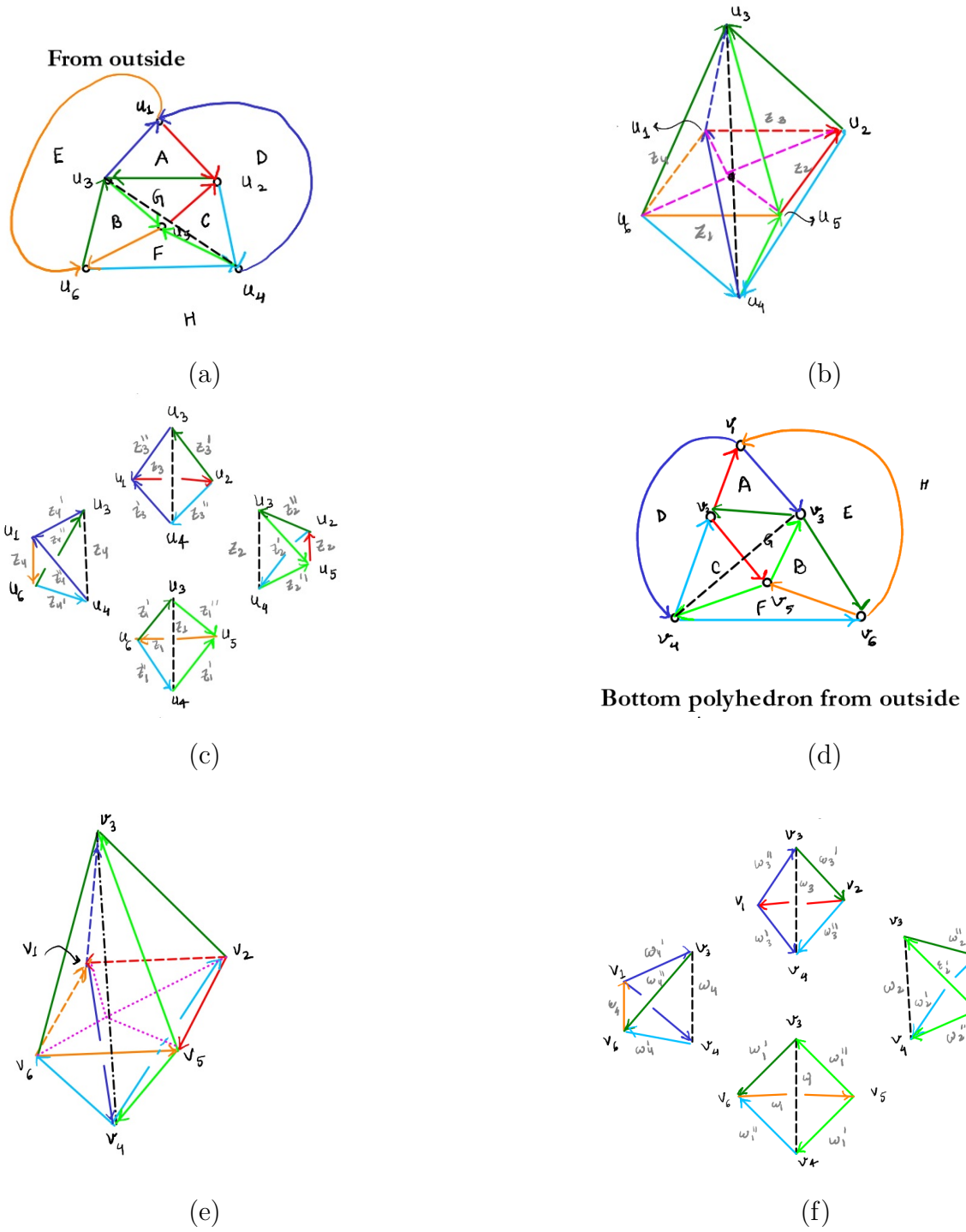

Figure 3.14: Triangulation of the top and bottom polyhedra of Borromean rings complement. Note that the edge (v_3, v_4) and (u_3, u_4) are dashed differently in (b) and (e), to signify a constructed edge and later on we use the regular dashed edge to represent v_3, v_4 and u_3, u_4 in (c) and (f).

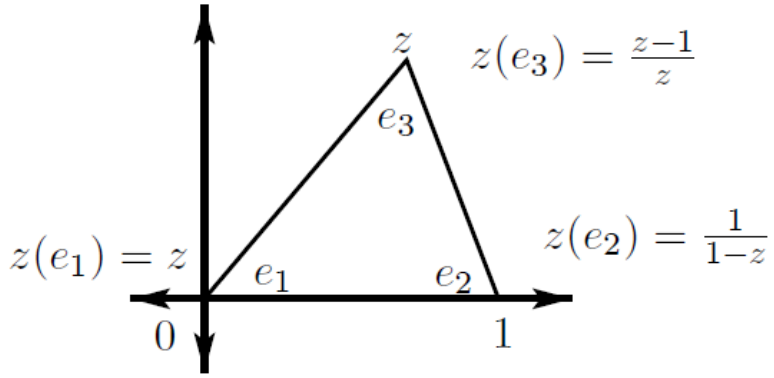

Figure 3.15: The edge invariants, image from [16]

ϕ, we can send one other vertex to 1 and the other to a $z' \in \mathbb{C}$. We assume that z' has a positive imaginary part, if not we can use an isometry to send it to a point with a positive imaginary part. We say that $z(e) := z'$ is the **edge-invariant** for the edge e. See Figure 3.15.

Lemma 3.4.1. *For a tetrahedron T, there are 6 edges. Let e_1 denote the edge running from 0 to ∞, the third vertex at 1 and the fourth one at z. Let e_2 denote the edge running from 1 to ∞ and e_3 be the edge running from z to ∞. Then, the edge invariants, $z(e_1), z(e_2), z(e_3)$ are related by the following relations:*

$$z(e_1)z(e_2)z(e_3) = -1 \text{ and}$$

$$1 - z(e_1) + z(e_2)z(e_3) = 0$$

Proof. We consider three cases for e_1, e_2 and e_3. *Case I* For e_1, we directly have that $z(e_1) = z$. *Case II* For e_2, we consider an isometry fixing ∞, $1 \mapsto 0$ and $z \mapsto 1$, i.e $w \mapsto \frac{w-1}{z-1}$. This isometry sends 0 to $\frac{-1}{z-1}$. Hence, $z(e_2) = \frac{-1}{z-1}$. *Case III* For e_3, consider the isometry fixing ∞, $z \mapsto 0$ and $0 \mapsto 1$, so it is given as $w \mapsto \frac{w-z}{-z}$, hence it sends 1 to $\frac{z-1}{z}$. The edge invariants therefore are,

$$z(e_1) = z; z(e_2) = \frac{-1}{z-1}; z(e_3) = \frac{z-1}{z}. \tag{3.1}$$

□

Now we consider the gluing of ideal tetrahedra. We fix an edge e of the gluing and let T_1 be the tetrahedron with edge e_1 glued to e. We put T_1 in $\mathbb{H}^3$ with edge e_1 from 0 to ∞, then the other vertices are 1 and $z(e_1)$. This gluing identifies each face of T_1 with another face in a different tetrahedron glued to e via edge e_2. Let F_1 denote the face with vertices $0, \infty, z(e_1)$, we wish to glue F_1 to a F' in T_2, so we use an isometry of $\mathbb{H}^3$ fixing points $0, \infty$ and sending $1 \mapsto z(e_1)$ and the other vertex to $z(e_1)z(e_2)$. We continue adding tetrahedra $T_3, T_4, ...$ in a similar fashion counter-clockwise. Eventually, we will end up with a tetrahedron T_n gluing to T_1. the vertices of this tetrahedron will be at $0, \infty, z(e_1)z(e_2)....z(e_{n-1})$ and $z(e_1)z(e_2)....z(e_n)$.

Theorem 3.4.2. *Let M^3 denote a topological ideal triangulation such that each tetrahedron has a hyperbolic structure. A hyperbolic structure on the gluing of the tetrahedra, resulting in M, is induced by the hyperbolic structure on each tetrahedron if and only if for each edge e, $\Pi z(e_i) = 1$ and $\sum arg(z(e_i)) = 2\pi$, where the sum and the product are over the edges that glue to e.*

Proof. We assume that the M^3 obtained from gluing ideal tetrahedra has a $(\text{Isom}(\mathbb{H}^3), \mathbb{H}^3)$-structure. So, every point $p \in M$ has a neighborhood isometric to a ball in $\mathbb{H}^3$. Consider a point on an edge. If it has a neighborhood isometric to a ball, then the sum of the dihedral angle about the edge must be 2π, i.e.$\sum arg(z(e_i)) = 2\pi$. Moreover, as the last face of the last tetrahedron should glue to the face of the first tetrahedra with vertices at $0, \infty, z(e_1)$ and 1, hence, $z(e_1)z(e_2)....z(e_n) = 1$ or $\Pi z(e_i) = 1$
Conversely, if we have that $\Pi z(e_i) = 1$ and $\sum arg(z(e_i)) = 2\pi$, then any point on the edge under the gluing has a 3-dimensional open disk isometric to a ball in $\mathbb{H}^3$. □

The equations in the Theorem 3.3.1 are known as the gluing equations for a particular edge e. Note that the $z_i's$ satisfying the gluing equations give a hyperbolic structure on M which is in general incomplete.

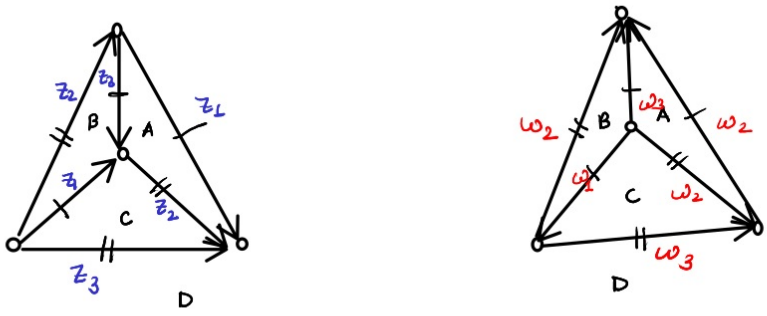

Figure 3.16: Ideal polyhedra associated with Figure-8 knot complement

Example 1 continued: Gluing equations for the Figure-8 complement

To calculate the gluing equations for the Figure-8 decomposition, we need to modify it a little bit. In the earlier construction, we were looking at the top polyhedra from the inside, now we need to look at it from the outside. See Figure 3.16. We assign complex numbers to each tetrahedron, z_1, z_2, z_3 and w_1, w_2, w_3, respectively. We divide edges into two classes, one with a single line through it and the other with two lines through it. We calculate edge invariants for each class and get the gluing consistency equations.
For the edge with a single line across, we get.

$$z_1 z_3 z_1 w_1 w_3 w_1 = 1 \text{ or } z_1^2 z_3 w_1^2 w_3 = 1$$

For the edge with two lines across it, we get,

$$z_2 z_2 z_3 w_2 w_3 w_2 = 1 \text{ or } z_2^2 z_3 w_2^2 w_3 = 1$$

Substituting $z_1 = z, w_1 = w$ and using equation 3.1, we get that

$$z^2 . \frac{z-1}{z} . w^2 . \frac{w-1}{w} = 1$$

this simplifies to,

$$z.(z-1).w.(w-1) = 1$$

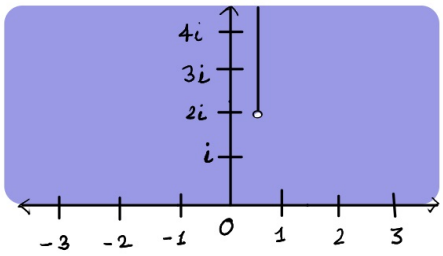

Figure 3.17: Solutions for gluing equations for Figure-8 complement.

Solving for z in terms of w,

$$z = \frac{1 \pm \sqrt{1 + \dfrac{4}{w(w+1)}}}{2}$$

For the triangulation to have a hyperbolic structure, we need to ensure that $Im(z), Im(w) > 0$ we see that solutions exist if $\sqrt{1 + \dfrac{4}{w(w+1)}}$ is not positive and real. Thus, the solutions for w can be parameterized as the space in Figure 3.17. One particular solution is $z = w = \dfrac{1}{2} + \dfrac{i\sqrt{3}}{2}$. We will see that this solution gives a complete hyperbolic structure to the Figure-8 knot complement.

Example 2 continued: Gluing equations for the Borromean rings complement

We now calculate the gluing equations for the Borromean rings' complement. We recall the triangulations of the top and bottom polyhedra from Figure 3.14. To each polyhedra, we assign complex numbers, $\{z_j, z'_j, z''_j\}$ and $\{w_j, w'_j, w''_j\}$ for $j = 1, 2, 3$, see Figure 3.18. We note that each collection, for a particular value of j, follows the equation 3.1. We read off the gluing equations for the edges of each color as:

$$z_1 z_2 z_3 z_4 w_1 w_2 w_3 w_4 = 1, \text{ Black edge}$$

$$z'_3 z''_3 z'_4 z''_4 w'_3 w''_3 w'_4 w''_4 = 1, \text{ Blue edge}$$

$$z_2 z_3 w_2 w_3 = 1, \text{ Red edge}$$

$$z'_1 z''_2 z'_3 z''_4 w'_1 w''_2 w'_3 w''_4 = 1, \text{ Dark green edge}$$

$$z''_1 z'_2 z''_3 z'_4 w''_1 w'_2 w''_3 w'_4 = 1, \text{ Light blue edge}$$

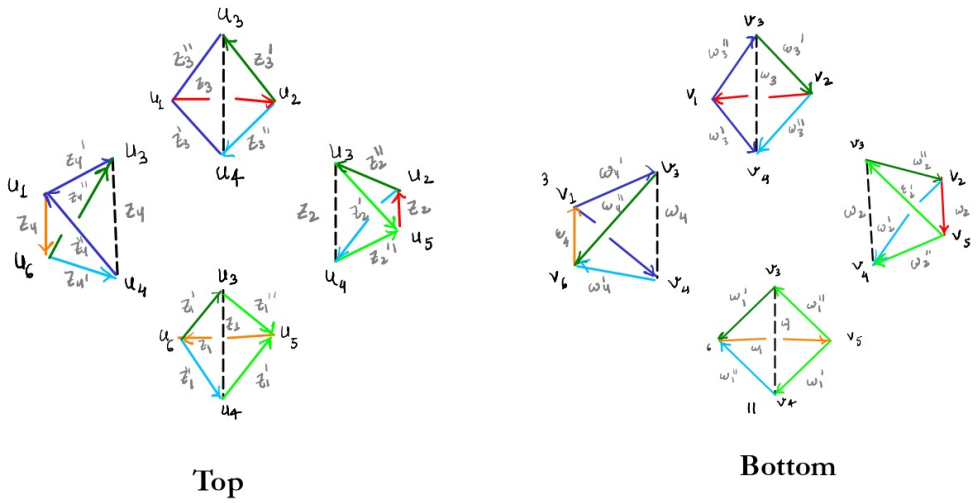

Figure 3.18: Triangulations of the top and bottom polyhedra.

$$z_1' z_1'' z_2' z_2'' w_1' w_1'' w_2' w_2'' = 1, \text{ Light green edge}$$

$$z_1 z_4 w_1 w_4 = 1, \text{ Orange edge}$$

We notice that one solution to the above equation is $z_j = w_j = i$, $z_j' = w_j' = \dfrac{i+1}{2}$ and $z_j'' = w_j'' = i + 1$, for $j = 1, 2, 3$. We will see that this solution corresponds to a complete hyperbolic structure on the link complement.

3.4.1 Completeness

Definition 3.4.2. *Let M be a 3-dimensional manifold with a torus boundary. We define a cusp or a cusp neighborhood of M to be the neighborhood of ∂M homeomorphic to the product $T^2 \times I$. A cusp torus is the torus component, i.e. the boundary component, of ∂M.*

Definition 3.4.3. *Let M have an ideal topological triangulation. We truncate the vertices of each ideal tetrahedron, we obtain a collection of triangles lying on the boundary of a cusp. The edges of the triangles inherit a gluing from the gluing of the faces of the tetrahedra, this results in a triangulation of each boundary torus. We call this triangulation a cusp triangulation.*

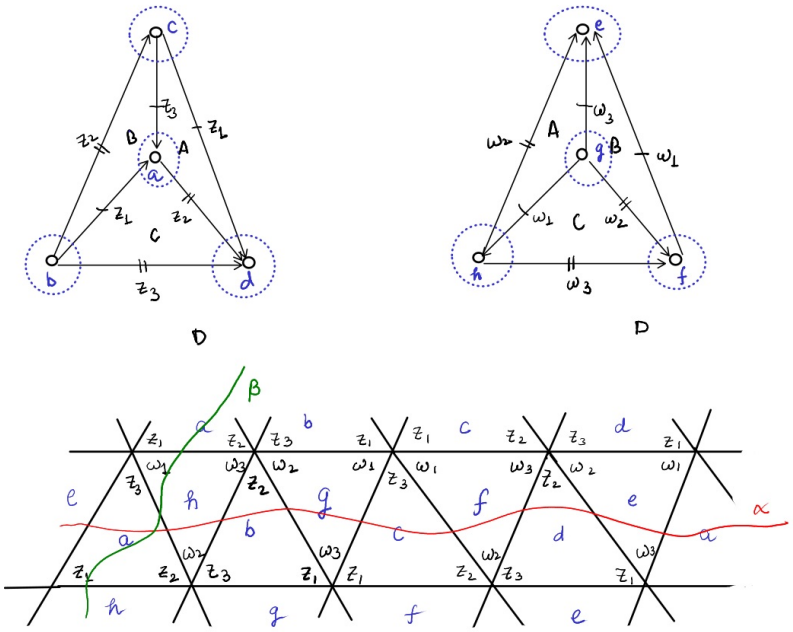

Figure 3.19: Cusp triangulation of the Figure-8 knot

Example 1 continued: the cusp triangulation of Figure-8 knot can be seen in Figure 3.19.

Theorem 3.4.3. *A 3-manifold M with a torus boundary with hyperbolic structure $(Isom(\mathbb{H}^3), \mathbb{H}^3)$ has a complete hyperbolic structure if and only if for each cusp of M, the induced structure on the boundary of a cusp is a Euclidean structure on the torus.*

Let M be a manifold with a topological ideal triangulation, and a hyperbolic structure such that gluing of the tetrahedra follows the Theorem 3.4.2. For the boundary T of a cusp of M and $[\alpha] \in \pi_1(M)$, we associate a complex number $H(\alpha)$ as follows:
The loop α is homotopically equivalent to a curve running monotonically through any triangle of the cusp triangulation. Denote the edge invariants of the corners cut off by α by $z_1, z_2, ..., z_n$. We also associate a value $\epsilon_i = \pm 1$ in the following way: $\epsilon_i = 1$ if the $i-th$ corner cut off by α lies to the left of α and $\epsilon_i = -1$ if the corner lies to the right of α. Now we define,

$$H(\alpha) = \prod_{i=1}^{n} z^{\epsilon_i}$$

Proposition 3.4.4. ***Completeness Equations*** *Let T denote the torus boundary of a cusp neighborhood of M, where M admits a topological ideal triangulation, and the ideal tetrahedra*

components of M admit hyperbolic structure and satisfy the edge gluing equations. Then let α, β be generators of $\pi_1(M)$. If $H(\alpha) = 1$ and $H(\beta) = 1$ are satisfied, then the ideal triangulation is a geometric ideal triangulation and hence the induced hyperbolic structure is complete.

Example 1 continued: For the cusp triangulation of the complement of the Figure-8 knot, Figure 3.19, consider the curve α, marked in red, we can write $H(\alpha)$ as,

$$H(\alpha) = z_3 w_2^{-1} z_2 w_3^{-1} z_3 w_2^{-1} z_2 w_3^{-1} = (\frac{z_2 z_3}{w_2 w_3})^2$$

There is another curve β in green running horizontally, for β,

$$H(\beta) = z_2^{-1} w_1 = \frac{w_1}{z_2}$$

Solving the equations $H(\alpha) = 1$ and $H(\beta) = 1$. Using the equation 3.1,

$$z(e_1) = z; z(e_2) = \frac{-1}{z-1}; z(e_3) = \frac{z-1}{z}.$$

$H(\alpha)$ simplifies as,

$$H(\alpha) = (\frac{-1}{(z-1)} \frac{(z-1)}{z} \frac{(w-1)}{-1} \frac{w}{(w-1)})^2 = (\frac{w}{z})^2$$

Simplifying $H(\beta)$, we get,

$$H(\beta) = \frac{w}{\frac{-1}{z-1}} = w(1-z)$$

Solving we get that $z = w$ and hence $z(1-z) = 1$ has a solution in the upper half plane, $z = w = \frac{1}{2} + \frac{i\sqrt{3}}{2}$.

Example 2 continued: Completeness equations for Borromean rings complement The structure obtained by joining the two polyhedra has three cusps. We take cusp triangulation of one cusp, the pink cusp in Figure 3.20 and calculate $H(\alpha)$ for $\alpha \in \pi_1(M)$, where M is a manifold with torus boundary and admits a topological ideal triangulation. The triangulation is given in Figure 3.21.

We consider three generators of the fundamental group, α, β, γ, and completeness equations

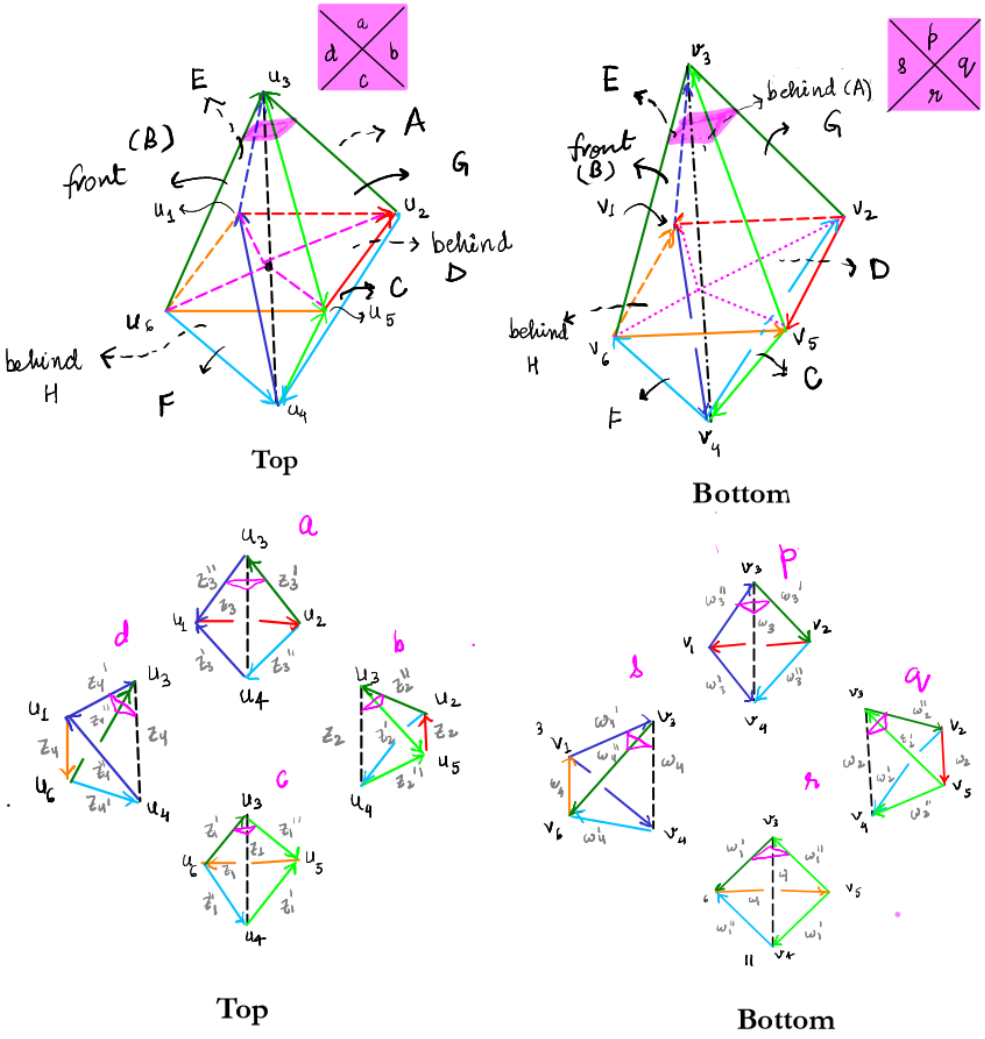

Figure 3.20: We write cusp triangulation of the cusp marked in pink.

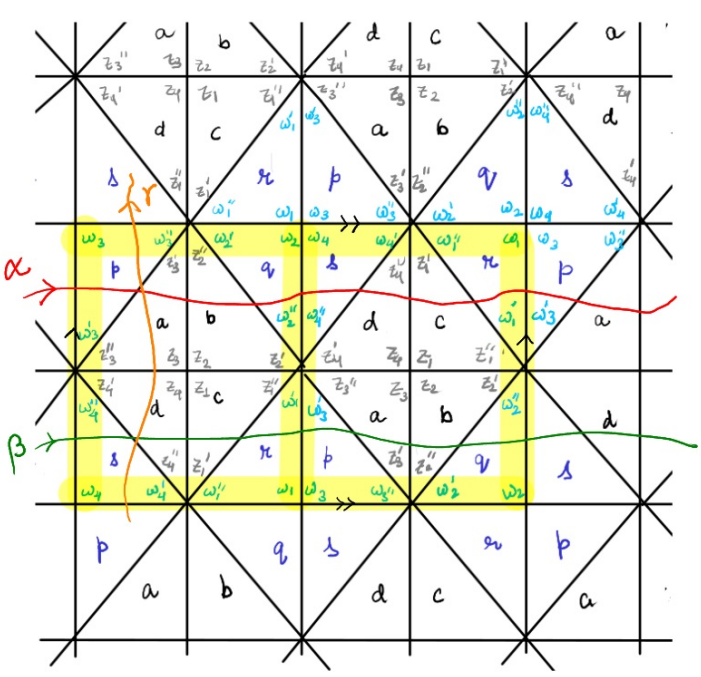

Figure 3.21: Cusp triangulation of the pink cusp marked in Figure 3.20; the fundamental domain is highlighted in yellow with the opposite sides identified.

for each curve are:

$$H(\alpha) = (w_3')^{-1} z_3' z_2'' (w_2'')^{-1} (w_4'')^{-1} z_4'' z_1' (w_1')^{-1} = 1,$$

$$H(\beta) = w_4'' (z_4'')^{-1} (z_1')^{-1} w_1' w_3' (z_3')^{-1} (z_2'')^{-1} w_2'' = 1,$$

and,

$$H(\gamma) = (w_4')^{-1} z_4' z_3'' (w_3'')^{-1} = 1$$

Solving the equations simultaneously with gluing equations gives the edge parameters and hence the complete hyperbolic structure. We observe that $z_j = w_j = i$, $z_j' = w_j' = \dfrac{i+1}{2}$ and $z_j'' = w_j'' = i+1$, for $j = 1, 2, 3$ satisfies both the gluing and completeness equations. Hence, it gives a complete hyperbolic structure on the complement of the Borromean rings.

Now, that we have a complete hyperbolic structure on the knot complements, we state some important results for the complete hyperbolic structures.

Theorem 3.4.5 (Mostow-Prasad rigidity)**.** *If M_1^n and M_2^n are complete hyperbolic n-manifolds*

with finite volume and $n \geq 3$, then any isomorphism of the fundamental groups $\phi : \pi_1(M_1) \to \pi_1(M_2)$ is realized by a unique isometry.

Theorem 3.4.6 (Gordon-Leucke Theorem)**.** *If two knots have complements that are homeomorphic by an orientation-preserving homeomorphism, then the knots are equivalent.*

Thus, a hyperbolic structure on a knot complement is a complete invariant of the knot.

Chapter 4

Right-angled volume

In this chapter, we discuss the right-angled volume of alternating link complements defined by Champanerkar, Kofman and Purcell in [6]. The exposition in this Chapter is based on their paper.

4.1 Background

Given an alternating link diagram, the link complement has a combinatorial polyhedral decomposition into polyhedra whose 1-skeleton is isomorphic to the projection of the link diagram [13]. Champanerkar, Kofman and Purcell [6] investigated when these combinatorial polyhedra can be given a hyperbolic structure and under what circumstances are the resulting hyperbolic polyhedra invariants of the alternating link. For a reduced, twist-reduced, prime alternating link diagram of a hyperbolic link they constructed right-angled ideal hyperbolic polyhedra using 3 different approaches - geometry, topology and combinatorics, and proved various properties of these hyperbolic polyhedra. In particular, they proved that the collection of these hyperbolic polyhedra is an invariant of the alternating link diagram, and is intrinsically related to the hyperbolic geometry of the link complement. The sum of the volumes of these right-angled ideal hyperbolic polyhedra is called the *right-angled volume* of the alternating link.

Below we define and explain the combinatorial construction of these right-angled ideal hyperbolic polyhedra. We also recall definitions and properties of link diagrams from Chapter 3, section 3.2.

4.2 Polyhedral decomposition of alternating link complements

We recall the decomposition of a knot complement into polyhedra from Chapter-3.

Theorem 4.2.1. *[16] The complement of an alternating link L can be obtained by gluing two ideal polyhedra P_1 and P_2 that satisfy the following:*

1. *P_1 and P_2 are obtained by labeling the boundary of 3-balls with the projection graph of*

L. One of the polyhedron is labeled from the inside and the other from the outside.

2. *All ideal vertices have degree 4. They correspond to the over-crossings in the top polyhedron and under-crossings in the bottom one.*

3. *Ideal edges correspond to crossing arcs in the diagram, and each edge class contains four edges, two each on each polyhedron.*

4. *Faces correspond to regions of the diagram, and are checkerboard colored.*

5. *Each face of the top polyhedron is glued to the identical face in the bottom polyhedron. The gluing rotates a face by one edge in a clockwise direction for white faces and rotates by one edge in an anticlockwise direction for the shaded faces.*

Let L be a link with reduced, prime, alternating diagram, and consider its associated checkerboard surfaces, white (W) and shaded (S). Then cutting $S^3 - K$ along both W and S simultaneously decomposes into two identical (topological) ideal polyhedra. We call either of these polyhedra the checkerboard polyhedron associated with the link diagram L. The checkerboard polyhedra satisfies the properties of the above theorem.

4.3 Combinatorics of link diagrams

Let L be a reduced, twist-reduced, prime alternating diagram of a link, let $\Gamma(L)$ denote its 4-valent projection graph and let $\Gamma^*(L)$ denote its planar dual.

Definition 4.3.1. *A k-circuit is a simple closed curve composed of k-edges of a graph G.*

We are interested in 4-circuits in $\Gamma^*(L)$ of a reduced, twist-reduced, prime alternating link diagram. We call a 4-circuit *trivial* if it bounds a single crossing on either side. See Figure 4.1.

Definition 4.3.2. *Two 4-circuits are crossing parallel if they differ only by passing on opposite sides of a single crossing. See Figure 4.1. Two circuits A and B are said to be parallel if there exists a sequence of 4-circuits $A_1 = A, A_2, A_3, ...A_n = B$ such that each A_j is crossing parallel to A_{j+1} for all $j = 1, \ldots n-1$. See Figure 4.2.*

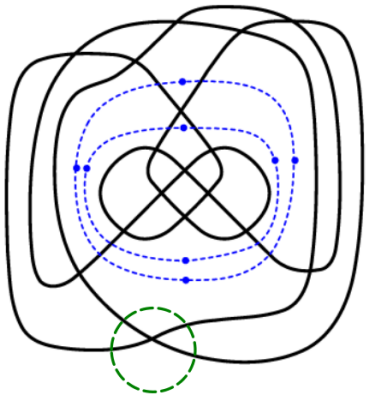

Figure 4.1: In blue: Two crossing-parallel 4 circuits; In green: A trivial 4-circuit, from [6].

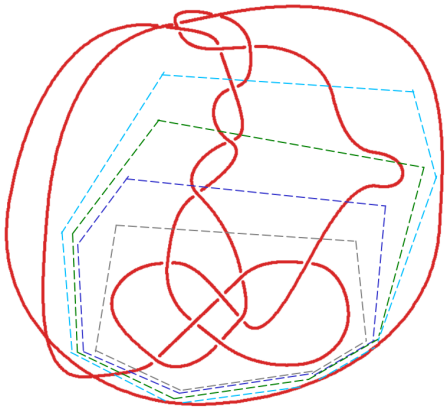

Figure 4.2: The gray(say A) and the light blue(say B) circuits are parallel with the sequence $A_1 = A, \text{blue}, \text{green}, A_n = B$, in a knot projection drawn in [7].

We can associate a punctured sphere to each 4-circuit by capping off the disks on either side of the projection plane, this results in a Conway sphere i.e. a sphere in S^3 which intersects the link in 4 points.

Lemma 4.3.1. *[6] Let A, B be 4-circuits in $\Gamma^*(L)$ with corresponding 4-punctured spheres $\bar{A}, \bar{B}$. Then the following are equivalent:*
(i) A and B are parallel.
(ii) $\bar{A}$ and $\bar{B}$ are ambient isotopic in $S^3 - L$.
(ii) A and B cobound a rational tangle diagram.

Definition 4.3.3. *1. A pair of parallel 4-circuits A and B is called a maximal bounding pair if A and B cobound a rational tangle diagram τ and there does not exist parallel circuits A', B' that cobound a rational tangle τ' such that τ is a subtangle of τ'.*

2. Two maximal bounding pairs $\{A, B\}$ and $\{A', B'\}$ are said to be disjoint if they cobound disjoint rational tangle diagrams.

See Figure 4.3, for an example of maximal bounding pairs of 4-circuits. The Figure also shows some 4-circuits, in red, that are not part of a maximal bounding pair.

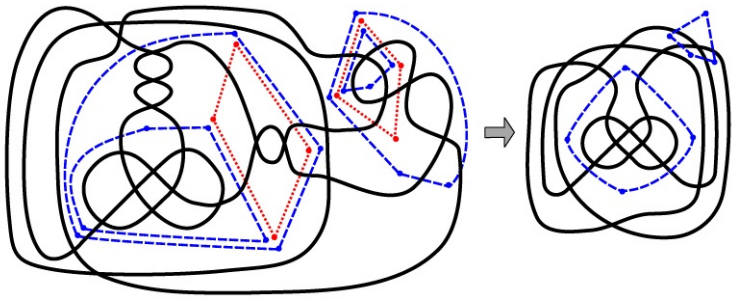

Figure 4.3: *Left* Two disjoint maximal bounding pairs of 4-circuits, shown in long dashed line in blue; *Right* Elimination of all crossings between both maximal bounding pairs via rational reduction; from [6]

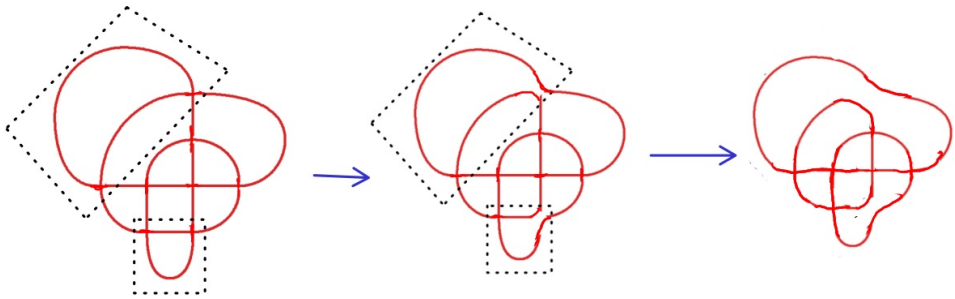

Figure 4.4: Rational reduction of the knot 8_{16} with the knot diagram from [7]

Rational Reduction of a link diagram

Definition 4.3.4. *Let L be as above. We look for all pairwise disjoint maximal bounding pairs of 4-circuits, and remove all crossings bound among each pair. In this step, each rational tangle with one boundary component gets replaced with a crossing and all crossings are removed from a rational tangle with two boundary components. We iterate this process, as some 4-circuits may become parallel after the first step. Since we remove some crossings at each step, the process ends with a diagram with no maximal bounding disjoint pairs. We call this resultant diagram as the rationally reduced diagram, and the process is called rational reduction of the diagram L.*

See Figure 4.4 for the rational reduction of the knot 8_{16}. In Chapter 5 we discuss the algorithm for rational reductions on Tait graphs of knot and link diagrams.

Definition 4.3.5. *A prismatic 4-circuit is a circuit γ such that no two edges of $\Gamma(K)$ that*

meet γ share a vertex in $\Gamma(K)$.

Lemma 4.3.2. *[6] Each non-trivial 4-circuit of a rationally reduced diagram of a link L is a prismatic 4-circuit.*

Proof. Let's assume to the contrary that there exists a 4-circuit such that its edges meet at a vertex, then the 4-circuit is adjacent to a crossing and we have a pair of crossing parallel 4-circuits, this contradicts the fact that the diagram is rationally reduced. □

Andreev's theorem

A combinatorial polyhedron P is a cell complex on S^2 that may be realized as a three-dimensional convex polyhedron. Steinitz's theorem characterizes undirected graphs (known as a polyhedral graph) formed by the 1-skeleton of a convex polyhedra as 3-connected simple planar graphs. Andreev's theorem characterizes a combinatorial polyhedron which can be realized as a right-angled ideal hyperbolic polyhedron with the same combinatorial structure as P with all the dihedral angles $\pi/2$.

Theorem 4.3.3. *[Andreev's theorem for 4-valent right-angled ideal polyhedra] A 4-valent combinatorial polyhedron admits a realization as a right-angled ideal hyperbolic polyhedron if and only if it has no nontrivial 4-circuits. The realization is unique up to isometry of $\mathbb{H}^3$.*

Hence, we can deduce the following for the projection graph Γ of a reduced, twist-reduced, prime, alternating link diagram K,

Lemma 4.3.4. Γ *admits a realization as a right-angled ideal hyperbolic polyhedron if and only if it has no non-trivial 4 circuits. This realization is unique up to the isometry of $\mathbb{H}^3$.*

Proof. From the Steinitz theorem, we have that Γ is a polyhedral graph if and only if Γ is 3-connected, simple and planar. Γ is simple if and only if it has no bigons and is 3-connected if it has no prismatic 4-circuits. Also, if Γ has no non-trivial 4-circuits then it has no bigons(as a result of the 3-connectivity). We therefore get the result from theorem 4.3.3. □

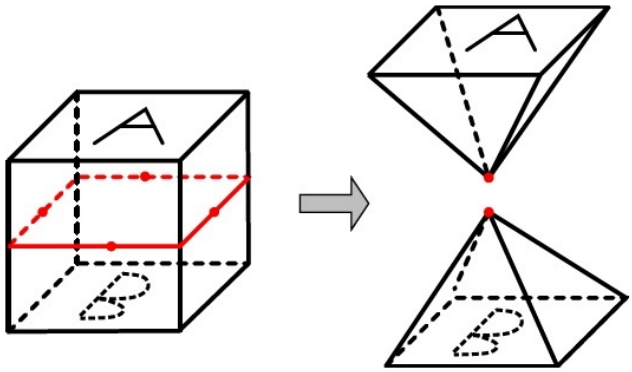

Figure 4.5: *Left*: A prismatic 4-circuit γ in red; *Right* Splitting the polyhedron along γ, $P//\gamma$, from [6].

Prismatic 4-circuit decomposition

Definition 4.3.6. *Let P be a 4-valent graph with no bigons, if γ is a prismatic 4-circuit for the dual graph P^*, then we define P split along γ or decomposition of P along γ, denoted by $P//\gamma$ as:*
We fix a planar embedding for P, and then from this plane graph, we construct two new graphs P_{int} and P_{ext}, where P_{int} (or P_{ext} respectively) consists of all edges and vertices of P in the bounded (or unbounded respectively) component of $\mathbb{R}^2 - \gamma$, such that P_{int} and P_{ext} each have four 1-valent vertices which were incident to γ. Let P_{int} (or P_{ext}) be the 4-valent graph obtained by capping off the four 1-valent vertices by a vertex lying in the bounded (or unbounded) region of $\mathbb{R}^2 - \gamma$. Then $P//\gamma$ is the disjoint union of P_{int} and P_{ext}. See Figure 4.5.

Definition 4.3.7. ***(Andreev Polyhedra)*** *Let L be a reduced, twist-reduced, prime, alternating link diagram. Let $\Gamma_r(L)$ denote the projection graph of its rationally reduced diagram. Then we split $\Gamma_r(L)$ iteratively along the non-trivial 4-circuits such that the resultant graphs are either,*

(i) have a single vertex, or

(ii) have non-trivial 4-circuits, or

(iii) have no non-trivial 4-circuits

We can apply Lemma 4.3.4 on graphs of case (iii). We discard all graphs of the case (i). Now, for the graphs of the case (ii), we pick a prismatic 4-circuit, decompose the graph along it, rationally reduce the components, and again look for 4-circuits and repeat the process, until we eventually end up with graphs with no non-trivial 4-circuits and we can apply Lemma 4.3.4 on it. The resulting set of the right-angled ideal hyperbolic polyhedra is called the Andreev polyhedra associated to L.

It is proved in [6] that the Andreev polyhedra are isomorphic to polyhedra constructed with a geometric approach called *guts polyhedra*, and are also isomorphic to polyhedra constructed using a topological approach called *tangle polyhedra*. The invariance under change in the link diagram follows from this equivalence. The other approaches are beyond the scope of this thesis.

Now we can talk about the hyperbolic volume of the Andreev polyhedra, known as the *right-angled volume*.

4.4 Right-angled volume

Now, with the Andreev polyhedra associated with a link, we define a geometric invariant for links, called the right-angled volume.

Definition 4.4.1. *Let L be a link with a reduced, twist-reduced, prime alternating diagram. The right-angled volume $vol^{\perp}(L)$ is defined to be twice the sum of the volumes of the Andreev polyhedra.*

Note that the factor of 2 in $vol^{\perp}(L)$ arises because in many cases the checkerboard polyhedra are twice the Andreev polyhedra.

The following is proved in [6] using the guts polyhedra:

Theorem 4.4.1. *[6] For any hyperbolic alternating link (L) with hyperbolic volume $vol(L)$, $vol^{\perp}(L) \leq vol(L)$.*

The $vol^{\perp}$ is computationally accessible via orthogonal circle packings, right-angled kites and Milnor's formula. Let L be a prime alternating link with a link diagram that is rationally

reduced and has no nontrivial 4-circuits. Let $\Gamma(L)$ be the projection graph of the link diagram. Fix any crossing c of L, and let $\mathcal{F}(c)$ be the closure of the four faces of $\Gamma(L)$ which meet c.

Theorem 4.4.2. *[6] Let G be the graph obtained by taking the central triangulation of each face of* $\Gamma(L)$ *that does not meet c, excluding the edges in* $\Gamma(L)$*. Then G can be realized as an Euclidean rectangle tiled by right kites, with one kite* k_e *for each edge e of* $\Gamma(L)$ *not in* $\mathcal{F}(c)$*. Let* θ_e *and* π - θ_e *denote the other kite angles of* k_e*. Then,*

$$vol^{\perp}(L) = 2\sum_{(e\in\Gamma(L)/\mathcal{F}(c))} \Lambda(\theta_e/2) + \Lambda((\pi-\theta_e)/2).$$

Note: Here

$$\Lambda(\theta) = -\int_0^{\theta} \log|2\sin t|dt$$

is the Lobachevsky function.

Example: Here is an illustration of the above Theorem. We compute $vol^{\perp}(L)$ for $L = W(4,3) = 9_{40}$, as shown in Figure 4.6 (a). Note that the knot does not have any bigons or prismatic 4-circuits so the projection graph $\Gamma(L)$ is already rationally reduced.

1. We pick a crossing c, as labeled in Figure 4.6 (a), and make it an ideal vertex. The resulting knot projection is depicted in Figure 4.6 (b).

2. As the projection is rationally reduced, we get right-angled hyperbolic structure of the complement, viewed from ∞ as Figure 4.6 (c), with the circles on $\partial\mathbb{H}^3$ corresponding to the geodesic faces.

3. We now subdivide the picture into a collection of 3/4 ideal tetrahedra by adding a vertical edge running from the center of each circle to infinity, and adding faces from this edge to the ideal vertices, as shown in Figure 4.6 (d). We see that there are right-angled kites in the rectangle.

4. Using trigonometry, we mark the sides and angles, as in Figure 4.6 (e).

5. Considering the 2×2 square, we see that $tan(\frac{\theta}{2}) = \frac{1}{z}$ and $z = \frac{1}{2}$, we get that $\frac{\theta}{2} = tan^{-1}(2)$, thus $\theta \approx 126.86989764°$.

Substituting the values of angles and using Theorem 4.4.2, we find that $vol^{\perp}(9_{40}) \approx 14.65544925$, and hence volume of each associated Andreev polyhedra is 7.327724625.

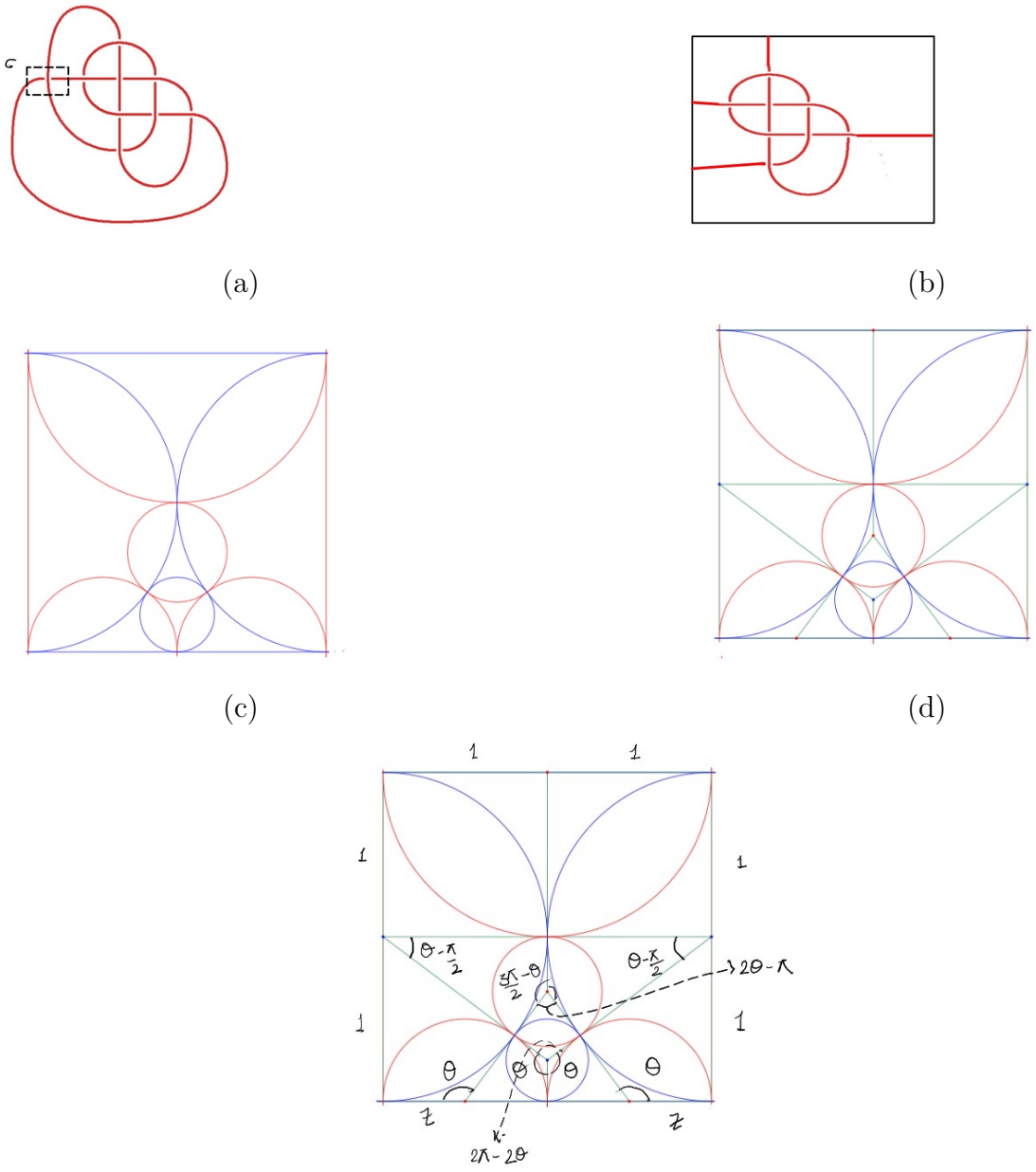

Figure 4.6: Decomposition of the right-angled polyhedron associated to 9_{40}: (a) on the knot projection of 9_{40} from [7] pick a crossing c to be an ideal vertex;(b) knot diagram with c at ∞; (c) associated right-angled polyhedra with faces in $\mathbb{H}^3$ and c at ∞, viewed from ∞; (d) joining center of circles of each color to divide the rectangle into right-angled kites;(e) the labeled angles.

Chapter 5

Algorithms and Computations

In this chapter, we generalize the procedure of rational reduction and prismatic 4-circuit decomposition to planar graphs and develop algorithms to check if planar graphs are rationally reduced and without prismatic 4-circuits. We extend the Felsner-Rote algorithm [9], implemented by Manfred Scheucher [17] to alternating knots and links.

5.1 Tait graphs

Let L be a link diagram which is a 4-valent plane graph with crossing information at every crossing. Let $\Gamma(L)$ denote a projection graph of L i.e. the 4-valent graph L without the crossing information. Since $\Gamma(L)$ is a 4-valent graph, the dual graph is a square graph (every face is a square) and hence bipartite. Every planar graph with all the faces of even length is bipartite [18]. Hence, we have a checkerboard coloring of the knot projection graph $\Gamma(L)$.

Definition 5.1.1. *The Tait graph G_L of a link diagram L is the signed plane graph whose vertices are the shaded faces of L, the edges correspond to crossings of L and the sign for every edge is assigned by the following rule:*

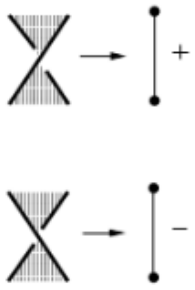

Figures 5.1 and 5.2 show the Tait graph of an alternating knot *K13a3* and a non-alternating knot respectively. The Tait graph construction has the following properties:

1) There are two choices for checkerboard coloring. If we choose the other coloring we obtain the planar dual G'_L with the edge signs reversed.

2) Reflecting all the crossings of the link results in the same Tait graph but with opposite signs for the edges. For alternating link diagrams we get the same sign on all edges, so we drop the signs.

3) Assuming the checkerboard coloring is chosen so that all edges are always positive, the Tait graph construction gives a bijection between planar graphs up to duality and alternating links up to reflection.

4) Tait graphs can have cut vertices, multiple edges, degree two vertices and pendant vertices depending on the link diagram.

5) Thistlethwaite [20] showed that for alternating link diagrams, the determinant of the link equals the number of spanning trees of the Tait graph.

5.2 Rational Reduction Algorithm

In Chapter 4, section 3, we described the operation of rational reduction for an alternating link diagram. In this section, we generalize this operation for Tait graphs of alternating links. The idea is to get to a 3-connected simple plane graph starting from G. We know that G is plane, we first need to make sure that all vertices have degrees greater than or equal to 3. Let L be a link with a reduced, twist-reduced, prime, alternating link diagram $\Gamma(L)$. Let G denote the Tait graph of L, and let G^* denote its dual.

Lemma 5.2.1. *1. There are no vertices of degree 1 in G.*
2. G has multiple edges or vertices of degree 2 if and only if L has bigons.
3. Rational reduction in L is equivalent to the following procedure in G: Collapse all multiple edges of G, we make G simple and whenever there is a vertex of degree 2, we contract one of the edges connecting the two vertices, and repeat the procedure again till we have no more vertices of degree less than 3 or all vertices of degree 2. The resulting graph is simple and either has all vertices of degree at least 3 or all vertices are degree 2.

Proof. For 1. we see that a vertex of degree implies a nugatory crossing in the knot projection graph, which is not possible as L is reduced.
Now, we first remove all multi-edges and loops in the graphs so that the resulting graph is simple. Now, we take the case of degree 2 vertices, we pick a vertex u of degree 2 and contract one of the edges containing u as one endpoint, and let its other endpoint be $\tilde{u}$. So, now we are left with one less vertex and a multi-edge at the vertex $\tilde{u}$. We remove the multi-edge. This procedure turns a bigon on $\Gamma(L)$ into a crossing. We repeat the procedure again and

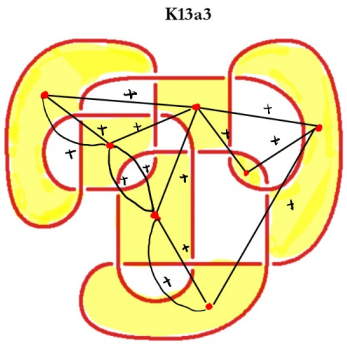

Figure 5.1: Tait graph of an alternating knot (a)*K13a3*, the knot projection from [7]

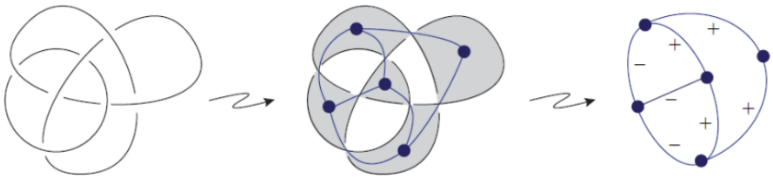

Figure 5.2: Tait graph of a non-alternating knot

we eventually end up with either all vertices of degree 2, in which case L is algebraic, or all vertices of degree greater than 2. Simultaneously, all bigons are replaced by crossings and then L gets rationally reduced. □

See Listing 5.1 for a schematic of the code to rationally reduce a given Tait graph.
Example: We take the example of the knot *K13a3*, See Figure 5.1, then the relabelled Tait graph looks like, $G = (V, E)$, where $V = (0, 1, 2, 3, 4, 5, 6)$ and $E = [(0, 1), (0, 1), (0, 2), (0, 6), (0, 6), (1, 2), (2, 3), (2, 5), (2, 6), (3, 4), (3, 5), (4, 6), (4, 6)]$. We remove all the multi-edges in G. We see that vertices $1, 4, 5$ have degree 2. We pick the vertex 1, we contract the edge $(1, 2)$, we relabel and again make sure that the graph is planar. We repeat the process again till we have no vertices of degree less than 3. This results in a graph $G' = (V', E')$, where $V' = (0, 1, 2)$ and $E' = [(0, 1), (0, 2), (1, 2)]$. Since all vertices in V' have degree 2, we realize that the knot projection *K13a3* is algebraic or rational and hence $vol^{\perp}(K13a3) = 0$.

Listing 5.1: Rational Reduction

input = A graph G
output = rationally reduced graph G'

```
def rational_reduction(G):
    G.remove_multiple_edges()
    degree = G.degree()
    if all(x <= 2 for x in degree)== True:
        return ('The link is algebraic, so rav = 0')
    else:
        deg_min = min(degree)
        u_min = degree.index(deg_min)
        if deg_min <= 2:
            v = max(G.neighbors(u_min))
            G.contract_edge((u_min,v))
            G.relabel()
            return rational_reduction(G)
    return G
```

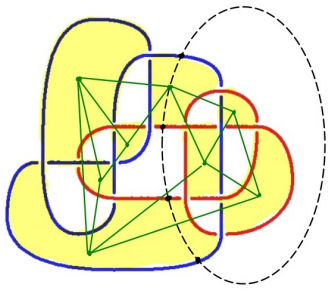

Figure 5.3: A link projection, from [7], and its Tait graph, the dashed circle represents a prismatic 4-circuit;

5.3 Prismatic 4-circuit decomposition algorithm

Lemma 5.3.1. *We begin with the Tait graph G of L. We consider the rationally reduced graph G' of G. A prismatic 4-circuit, say γ, of G is a cut-set $\{u, v\}$ of size two in the rationally reduced graph G'. Hence, decomposing $\Gamma(L)$ along γ is equivalent to decomposing G' along $\{u, v\}$ as: We cleave G' about $\{u, v\}$, i.e. we cut u and v from G, it disconnects the graph into two components H_1 and H_2, we add the vertex u, v to both components again.*

Proof. Let L be a reduced, twist reduced, prime alternating, rationally reduced link with the projection graph $\Gamma(L)$ and Tait graph G. See Figure 5.3 for an example. We look

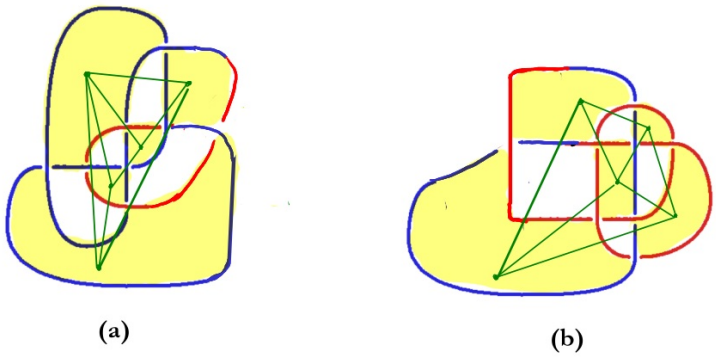

Figure 5.4: Components following prismatic decomposition.

for a prismatic 4-circuit, say γ in $\Gamma(L)$. We notice that γ travels alternatively between shaded and unshaded regions. Therefore, we see that in the Tait graph G, only two vertices corresponding to γ are there. These vertices form a cut-set. Now, we cut along the cut-set and add back these vertices to the components, G_1 and G_2. Then, we draw the medial graphs of the components to get the corresponding link, say L_1 and L_2. See Figure 5.4 (a), (b). Following the discussion from section 4.3, we also see that these are equivalent to the regions L_{ext} and L_{int} contained in $L//\gamma$.
If the projection graph $\Gamma(L)$ has multiple prismatic 4-circuits, then we repeat the above process for each component. This results in a collection of 3-connected simple planar graphs.
□

See Listing 5.2 for a schematic of the code for finding a prismatic 4-circuit and if present, decomposing the graph along it to give the components.
Example: Consider the example of the link *L14a21316*, see Figure 5.3. Note that the projection graph is rationally reduced, so any non-trivial 4-circuit is a prismatic 4-circuit. The circuit marked by black in Figure 5.2 is a prismatic 4-circuit. The Tait graph is $G = (V, E)$, where $V = (0, 1, 2, 3, 4, 5, 6, 7)$ and $E =$[(0, 1), (0, 2), (0, 5), (0, 6), (0, 7), (1, 3), (1, 4), (2, 3), (2, 4), (3, 4), (4, 6), (4, 7), (5, 6), (5, 7)]. Since the graph already has very vertex of degree greater than 2. We note that $\{3, 7\}$ is a cut-set of size 2. We cleave G along this cut-set into two components, G_1, G_2; here $V(G_1) = 0, 1, 2, 3, 4$ and $E(G_1) =$ [(0, 1), (0, 2), (0, 3), (1, 3), (1, 4), (2, 3), (2, 4), (3, 4)] and $V(G_2) = 0, 1, 2, 3, 4$ and $E(G_2) =$ [(0, 1), (0, 2), (0, 3), (1, 3), (1, 4), (2, 3), (2, 4), (3, 4)]. Both these components are 3-connected simple planar graphs.

Listing 5.2: Prismatic 4-circuit Decomposition

input = two copies of a graph G
output = A list of components after prismatic 4-circuit decomposition

```
def decomposition(G1, G2):
    rational_reduction(G1)
    rational_reduction(G2)
    cutsets = cutsets(G1)
    if all(x ==2 for x in G1.degree()) == True:
        b = G2
        a = {b.copy(immutable = True)}
    else:
        if all(len(y) == 2 for y in cutsets) == True:
            e = random.choice(cutsets)
            S_0,C_0,f_0 = G2.cleave(e)
            complist = []
            for g1 in S_0:
                g1.relabel()
                rational_reduction(g1)
                if all(x >=2 for x in g1.degree()) == True:
                    complist.append(g1)
                else:
                    g1 = decomposition(g1,g1)
                a =  complist
        else:
            b = G1
            a = {b.copy(immutable=True)}
    return a
```

5.4 Computing right-angled volume

As earlier, we will consider a link L with a reduced, twist-reduced, prime alternating link diagram. We consider its Tait graph G. We rationally reduce the graph G to get the graph G'. Then, we decompose G' along prismatic4-circuits, if there are any. Consequently, we end up with a collection of graphs that are 3-connected simple plane graphs. Now, we recall the Felsner-Rote algorithm [9] from Chapter 1 section 1.6 for 3-connected simple plane graphs. We now apply Felsner-Rote algorithm, implemented by Manfred Scheucher [17], on each graph to get a collection of radii, and hence by equation 1.1, a collection of angles corresponding to the vertices of the graph. We then use the theorem 4.4.1, [6] to compute the right angles volume of L. Listing 5.3 gives a schematic of the same.

Listing 5.3: Right angled volume calculator

input = A link L
output = $vol^{\perp}(L)$

```
G = L.white_graph()
rational_reduction(G)
list = decomposition(G,G)
rav = 0
for graph in list:
    radii = Felsner-Rote(graph)
    L = lambda x: -ln(abs(2*sin(x)))
    for x and y distict vertices in G^{\diamond}:
        theta = atan(r_y/r_x)
        L1 = integrate.quad(L, 0, theta)[0];
        L2 = integrate.quad(L, 0, (np.pi/2 - theta))[0]
        rav = rav + 2*(L1 + L2)
return rav
```

Example 1: We consider the case of knot 9_{40}, Figure 4.3 (a), we saw in Chapter 4 section 4.4. The Tait graph of the knot is $G = (V, E)$, where $V = (0, 1, 2, 3, 4)$ and edges $E = [(0, 1), (0, 2), (0, 3), (0, 4), (1, 2), (1, 3), (2, 3), (2, 4), (3, 4)]$. We notice that the knot diagram is already rationally-reduced and has no prismatic 4-circuits. So, we may apply Felsner-Rote algorithm to G directly. Doing so, we get the radii associated to each vertex of the angle graph $G^{\diamond}$ and the angles at each kite as depicted in Listing 5.4. Using these to compute the right-angled volume, we get that $vol^{\perp}(9_{40}) = 14.655383489158424$.

```
 radii = [0.93702257, 0.97098554, 1.60301741, 1.60300865, 0.40074192,
1.07019846, 0.80148838, 0.56204041, 0.8014961,  1.60303025, 0.53432392]
 angles = [1.10715886347028, 0.785402169210728, 1.249054316223814,
1.107152822635585, 0.7854049003874463, 1.249052677551538,
1.1071509792202805, 1.1071548351539349, 0.9272964363446556]
```

Listing 5.4: Radii and angles for Example 1

Example 2: We described the rational reduction and prismatic 4-circuit decomposition of the Tait graph of the link $L14a21316$ is described in the example discussed in section 5.3. Since G_1 and G_2 are the same after relabelling, we calculate the right-angled volume for G_1. Since, it is a 3-connected simple, plane graph, we may directly apply Felsner-Rote algorithm. We get the radii associated with each vertex of $G_1^\diamond$ and $G_2^\diamond$ as shown in Listing 5.5. Now, we use Milnor's computation to see that right-angled volume of G_1 is 12.046095791145135, and therefore $vol^\perp(L14a21316) = 24.092183999045186$

```
radii_1 = [0.91366202 0.84824942 0.82902495 0.82903188 1.6580488
0.71219724 1.17241967 1.51918091 1.17242025 0.58621046]
angles_1 = [0.9553171590273072, 0.955315579145558, 0.9553134481936485,
0.9553195203380521, 0.9553157632794393, 0.9553155329144003,
1.2309585153927813]
radii_2 = [0.96358922 0.8671485  0.59121734 1.18244205 1.18243891
0.61983438 0.83610515 0.83610194 1.37389541 1.67222007]
angles_2 = [0.9553152469167293, 0.9553134376645441, 1.2309603387599217,
 0.9553227361155744, 0.9553150627060404, 0.95531967158612,
0.9553163179969819]
```

Listing 5.5: Radii and angles for Example 2

We computed the right-angled volume for the alternating knot census: knots with crossings up to 12 from knotinfo [11], 13 to 15 from snappy [7] and 15 to 17 from Regina database [5]. We computed the $vol^\perp$ for about 2,304,756 knots and links.

We observe the first non-zero right-angled volume for knots with 8 crossings. See tables 5.1 through 5.3 for the non-zero $vol^\perp$ values for knots with crossings 8, 9, and 10. The $vol^\perp$ values for the knots with crossings 11 to 17 and for links with crossings 4 to 14 may be found here.

Table 5.1: Non-zero $vol^{\perp}$ of knots with 8 crossings.

Knot(K)	$vol^{\perp}(K)$
8_{16}	7.327724753417755
8_{17}	7.327724753417755
8_{18}	12.046091831710571

Table 5.2: Non-zero $vol^{\perp}$ of knots with 9 crossings.

Knot	$vol^{\perp}$
9_{29}	7.327724753417755
9_{32}	7.327724753417755
9_{33}	7.327724753417755
9_{34}	12.046091831710571
9_{38}	7.327724753417755
9_{39}	7.327724753417755
9_{40}	14.65544925012298
9_{41}	7.327724753417755

Table 5.3: Non-zero $vol^{\perp}$ of knots with 10 crossings.

Knot	$vol^{\perp}$
10_{82}	7.327724753417755
10_{84}	7.327724753417755
10_{85}	7.327724753417755
10_{86}	7.327724753417755
10_{87}	7.327724753417755
10_{88}	7.327724753417755
10_{90}	7.327724753417755
10_{91}	7.327724753417755
10_{93}	7.327724753417755
10_{94}	7.327724753417755
10_{98}	7.327724753417755
10_{100}	7.327724753417755
10_{101}	7.327724753417755
10_{102}	7.327724753417755
10_{103}	7.327724753417755
10_{104}	7.327724753417755
10_{105}	7.327724753417755

$vol^{\perp}$ of knots with 10 crossings.

Knot	$vol^{\perp}$
10_{106}	7.327724753417755
10_{107}	7.327724753417755
10_{108}	7.327724753417755
10_{109}	7.327724753417755
10_{110}	7.327724753417755
10_{112}	12.04609211314172
10_{114}	12.046091831710571
10_{115}	12.046091831710571
10_{116}	12.04609229334576
10_{117}	12.04609248915662
10_{118}	12.046091970185126
10_{119}	12.04609192683704
10_{120}	12.04609229334576
10_{121}	14.655449478268698
10_{122}	14.655448445153974
10_{123}	16.27577041129425

Table 5.5: $vol^{\perp}$ of links upto 8 crossings.

Link	$vol^{\perp}$
L6a4	7.327724753417755
L7a1	7.327724753417755
L8a1	7.327724753417755
L8a7	7.327724753417755
L8a16	7.327724753417755
L8a19	7.327724753417755

Table 5.6: $vol^{\perp}$ of links with 9 crossings.

Link	$vol^{\perp}$
L9a2	7.327724753417755
L9a10	7.327724753417755
L9a19	7.327724753417755
L9a20	12.046091970185126
L9a21	7.327724753417755
L9a22	7.327724753417755
L9a32	7.327724753417755
L9a42	7.327724753417755
L9a46	7.327724753417755
L9a51	7.327724753417755
L9a53	7.327724753417755

$vol^{\perp}$ of links with 10 crossings.

Link	$vol^{\perp}$
L10a4	7.327724753417755
L10a14	7.327724753417755
L10a20	7.327724753417755
L10a22	7.327724753417755
L10a23	7.327724753417755
L10a24	7.327724753417755
L10a42	7.327724753417755
L10a43	7.327724753417755
L10a49	7.327724753417755
L10a50	7.327724753417755
L10a51	7.327724753417755
L10a52	7.327724753417755
L10a53	12.04609211314172
L10a54	7.327724753417755
L10a55	7.327724753417755
L10a56	17.22483096769729
L10a70	14.655448445153974
L10a71	12.046092085254127
L10a76	7.327724753417755
L10a77	7.327724753417755
L10a78	7.327724753417755
L10a79	7.327724753417755
L10a80	7.327724753417755

$vol^{\perp}$ of links with 10 crossings.

Link	$vol^{\perp}$
L10a86	12.04609192683704
L10a104	7.327724753417755
L10a106	7.327724753417755
L10a107	7.327724753417755
L10a111	14.655448534205256
L10a112	12.04609248915662
L10a113	7.327724753417755
L10a121	7.327724753417755
L10a127	7.327724753417755
L10a135	7.327724753417755
L10a137	7.327724753417755
L10a138	7.327724753417755
L10a140	7.327724753417755
L10a141	7.327724753417755
L10a147	7.327724753417755
L10a149	7.327724753417755
L10a155	7.327724753417755
L10a156	12.046092019218287
L10a157	7.327724753417755
L10a158	7.327724753417755
L10a163	12.046092019218287
L10a164	7.327724753417755
L10a169	14.65544950683551
L10a173	7.327724753417755

5.5 Weaving Knots

A weaving knot $W(p, q)$ is the alternating knot or link with the same projection as the standard closed p-braid $(\sigma_1\sigma_2.....\sigma_{p-1})^q$ diagram of the torus knot or link $T(p, q)$. Since weaving diagrams are reduced, alternating, the crossing number of $W(p, q)$ is $(p - 1)q$. Weaving

knots are special in the sense that their projection graph is rationally reduced and has no non-trivial 4-circuits. Hence, its Tait graph is always simple, planar and 3-connected, and we may apply Felsner-Rote algorithm on the Tait graphs using Scheucher's implementation of the code [17]. The knot 9_{40} in Example 1 of the previous section is the weaving knot $W(4,3)$.

Although the implementation of Scheucher's code for weaving knots and links was straightforward, we encountered problems in the numerical accuracy part. We briefly describe how the errors and bugs were detected and fixed. The implementation produced consistent monotonic right-angled volume initially; but as the graph size increased, the value was irregular, i.e $W(3,23) = 83.83884533$, $W(3,24) = 87.52061827$, $W(3,25) = 91.20012264$, $W(3,26) = 80.7615542$. Upon debugging the code, we see that the radii obtained after implementing Scheucher's implementation of the Felsner-Rote algorithm that uses the optimizer $scipy.optimize.minimize((func, x0, jac = quality\_der, method =' BFGS'))$ with an appropriate $func = quality$, we observe that the some the radii are negative, see Listing 5.6 which is contrary to our assumption of the radii being non-negative.

```
    radii = [ 1.00000000e+00  1.00000000e+00  1.41514350e+00 -1.65659311e
   +00
  3.65804920e-01  4.25067425e-01  1.53118901e-01  4.72383513e-02
  4.79891133e-02  2.62849628e-02  1.16907527e-02  1.75632410e-02
  3.52425078e-02  3.87276516e-02  3.37512485e-02  3.46025616e-02
  4.00809689e-02  3.72358232e-02  1.65660151e-02  1.06280658e-02
  2.61526550e-02  4.80127618e-02  4.76264071e-02  1.53087789e-01
  4.25089131e-01  3.65853807e-01 -1.65659404e+00  1.00000000e+00
 -3.75375622e-02  1.00000000e+00 -3.75306311e-02  1.19651662e-03
  4.14365647e-01  3.82111992e-01  2.33319011e-02  5.57714888e-02
  3.99180794e-02  1.77408702e-02  1.29272723e-02  2.30704008e-02
  3.12294677e-02  2.67085468e-02  3.05355913e-02  2.53038503e-02
  2.96724598e-02  2.10522972e-02  1.07325817e-02  1.72269416e-02
  4.02834631e-02  5.60653963e-02  2.34347139e-02  3.82034541e-01
  4.14397138e-01  1.22813034e-03]
  rav = 80.7615542
```

Listing 5.6: Radii using the method BFGS

Hence, the angle calculations and hence the right-angled volume are not accurate. To resolve this, we tried out different methods for $scipy.optimize.minimize((func, x0, jac = quality\_der, method =''))$ from the SciPy package, namely, "Nelder-Mead, Powell, SLSQP,

trust-constr, L-BFGS-B", see listings 5.6 to 5.12. The method "Nelder-Mead" still produces some radii with negative values. The method "TNC" overshoots the right-angled value, better approximates are from the method, "L-BFGS-B", "Powell", "SLSQP" and "trust-constr". We use the method "SLSQP" for further calculations of the right angled volume.

```
   radii = [ 0.94586369 -0.12121557  7.2823447   0.5557858   1.10679958
  0.44093994
 0.40955114  1.47898447  1.50955803  0.48956313  0.46094224  0.27867887
 1.46216004  1.21967032  0.12460586  0.23127892  1.09287621  0.9622461
 0.55719187  0.68946394  1.87935192  1.95199163  0.57954473  1.32185782
 0.54060097  0.11838955  0.14665587  4.80962715  0.33758717 -0.26032173
 3.08895728  0.65231321  0.68870973  0.35249967  0.74029796  1.28975943
 0.98561684  0.50875733  0.33743823  0.3421332   1.87941247  0.29089158
 0.11840429  0.632743    0.89124822  0.87266385  0.48229917  0.91710838
 3.27463235  0.67934518  0.64723971  1.03159646  0.18156328  0.10867042]
 rav = 97.11420328511566
```

Listing 5.7: Radii using the method Nelder-Mead

```
radii = [1.          1.          6.27093022 1.59084598 0.5407582
  0.27857183
0.17402234 0.12208191 0.09275558 0.07481211 0.06328968 0.05573688
0.05084861 0.04790098 0.04650451 0.04648944 0.04785505 0.05076805
0.05561568 0.06312054 0.07459335 0.09249087 0.12177363 0.17364305
0.27804274 0.53988763 1.58881111 1.         3.156169   1.
3.15863505 0.80124521 0.36498968 0.21263188 0.14243037 0.10463945
0.08221466 0.06806857 0.05884022 0.05279232 0.04897125 0.04684882
0.04615824 0.04681873 0.04890924 0.05269322 0.05869732 0.06787617
0.08197607 0.10435722 0.14210059 0.21220537 0.36436995 0.80015186]
rav = 94.88485146268373
```

Listing 5.8: Radii using the method L-BFGS-B

```
radii = [1.          1.          5.89858343 0.47560253 0.59588741
  0.54452493
0.60797564 0.75036017 0.69844693 0.60152964 0.60263472 0.62805703
0.64831109 0.58110818 0.61369396 0.60356544 0.58417504 0.55286337
0.6059227  0.57923444 0.58068117 0.6817292  0.603688   0.64209548
0.73000903 0.60083963 0.52696185 1.         0.74400164 1.
0.68878715 0.4995869  0.52331503 0.50335823 0.6773806  0.65926697
0.60442456 0.5556171  0.56477908 0.61969388 0.58743848 0.56289207
0.56874277 0.60012    0.50065786 0.55871176 0.56809103 0.54152801
```

```
0.59714939 0.59562859 0.57139519 0.66510595 0.62443231 0.50132529]
rav =  104.00413394070397
```

Listing 5.9: Radii using the method TNC

```
radii =  [4.29827949e+04 4.29827949e+04 1.57744322e+01 3.56195969e+00
1.11978535e+00 5.76275917e-01 3.95780434e-01 3.24904835e-01
2.89677368e-01 2.61226556e-01 2.27157629e-01 1.88233965e-01
1.52443059e-01 1.26990590e-01 1.12238658e-01 1.07389080e-01
1.10646625e-01 1.22062812e-01 1.41133279e-01 1.71108282e-01
2.19509900e-01 2.84832669e-01 3.85877682e-01 5.52138396e-01
8.24914760e-01 1.48085769e+00 4.12552959e+00 4.29802069e+04
8.05662007e+00 4.29802069e+04 7.46073385e+00 1.73353075e+00
7.50854159e-01 4.57827949e-01 3.49060829e-01 3.02232917e-01
2.73083564e-01 2.43251282e-01 2.06407790e-01 1.68523403e-01
1.37755648e-01 1.17866918e-01 1.08338013e-01 1.07687208e-01
1.14960283e-01 1.30009088e-01 1.53559400e-01 1.91879115e-01
2.47441463e-01 3.25895056e-01 4.52678207e-01 6.53095171e-01
1.03403414e+00 2.12160922e+00]
rav =  95.07046621400607
```

Listing 5.10: Radii using the Powell method

```
radii =  [1.          1.          7.63608273 1.93730786 0.65910493
  0.33968468
0.21215391 0.14871566 0.11286536 0.09093996 0.07684138 0.06761028
0.06162947 0.058014   0.05629464 0.05626365 0.05791505 0.06146575
0.0673905  0.07655754 0.09054721 0.1123846  0.1481322  0.21139995
0.33867913 0.65794107 1.93665947 1.          3.84594335 1.
3.84569467 0.97614774 0.44497677 0.25926464 0.17358174 0.12740271
0.09999397 0.08269186 0.07140431 0.06401326 0.0593327  0.05672425
0.05586948 0.05666186 0.05920258 0.06382284 0.07116209 0.08236393
0.09955243 0.12687991 0.17293447 0.25842431 0.44395581 0.97505609]
rav =  94.88111820102203
```

Listing 5.11: Radii using the method SLSQP

```
radii =   [1.          1.          9.16823458 2.32587111 0.79060764
  0.40713379
0.25414509 0.17810594 0.13516782 0.10891065 0.09206527 0.08103316
0.07389792 0.06960273 0.06757993 0.06757991 0.06960265 0.07389777
0.08103291 0.09206487 0.10891006 0.13516694 0.17810463 0.25414314
0.40713086 0.79060301 2.32586193 1.          4.61779963 1.
```

```
4.61781089  1.1714778   0.53356478  0.31066085  0.20791053  0.15257384
0.11974751  0.09905453  0.08556922  0.07673764  0.07116337  0.06807641
0.06708717  0.06807636  0.07116326  0.07673744  0.0855689   0.09905405
0.1197468   0.15257278  0.20790897  0.31065855  0.53356136  1.17147237]
rav =  94.88029975216075
```

Listing 5.12: Radii using the method trust-constr

We give below a list of some right-angled volumes of weaving links $W(p, q)$ for $p = 3$ and $3 \leq q \leq 100$. We have additional datasets for $4 \leq p \leq 11$, here.

Link	$vol^{\perp}$
3	7.327724753417755
4	12.046146338555006
5	16.27563562165595
6	20.29860934683124
7	24.212035432250957
8	28.061314354713037
9	31.866404095149765
10	35.64373861140518
11	39.39953429637705
12	43.13807403534111
13	46.86569671222266
14	50.58636156551904
15	54.29712228799782
16	58.002534017911785
17	61.70379180142566
18	65.40006370368211
19	69.09164750096309
20	72.78287954871928
21	76.46988405209022
22	80.15535568251505

Link	$vol^{\perp}$
23	83.83891054393813
24	87.52098892581776
25	91.20279974608016
26	94.88042627074088
27	98.55786409482792
28	102.62850138919838
29	105.8224507322706
30	109.59014600795186
31	113.32293655681856
32	117.03665930604926
33	120.75992940715491
34	124.48010207667149
35	128.99267373391731
36	132.10056069679922
37	136.5197768531991
38	139.9710636886504
39	144.7126972137685
40	147.8125463548448
41	151.14096055364047
42	155.13112517819283

Link	$vol^{\perp}$
43	158.34012777141598
44	161.8123134161163
45	165.94845434566437
46	169.84788807560358
47	173.38441325016635
48	177.6896146421684
49	182.550572036822
50	185.6131226758073
51	189.3775225407
52	192.51161063025395
53	196.355245351833
54	200.00526649193765
55	203.4717259516048
56	207.48224774618305
57	211.4452457842173
58	215.50653836573304
59	219.11684637106583
60	223.0575397971553
61	226.97266412419123
62	230.76756404097964
63	235.1113179525159
64	237.84841286829803
65	241.58032052726372
66	245.3704066074261
67	248.851457850732
68	252.7657599529598
69	256.98261121415203
70	260.127175223649

Link	$vol^{\perp}$
71	263.9808839412878
72	267.77074338214186
73	271.13724817062086
74	274.9785126386003
75	278.7233218271037
76	282.3614892501607
77	286.0970091563437
78	289.68585495863823
79	292.7913173118408
80	297.62617438756143
81	300.3958853763038
82	304.04582169774227
83	307.52601787516016
84	311.5143920690465
85	315.4838118934473
86	319.37237340442243
87	323.80533262692586
88	326.8637538753727
89	330.5382569273061
90	335.21227718003547
91	338.6413391358324
92	342.35117332943776
93	345.3783453788652
94	348.9182540660048
95	352.5945437738851
96	356.6072640697381
97	360.1224499250706
98	364.2218611745339
99	367.69691768202017
100	371.5394634103089

Chapter 6

Patterns and Results

The content of this chapter includes the patterns and analysis of the generated data set of right-angled values of knots, links, and weaving knots using the algorithms described in Chapter 5.

6.1 Volume of right-angled polyhedra

We recall Definition 4.4.1 that $vol^{\perp}(L)$ is twice the sum of the volumes of the associated Andreev polyhedra. Egorov and Vesnin, [23] in 2020 computed the volumes of the ideal right-angled three-dimensional hyperbolic polyhedra with at most 23 faces [23]. With our calculation of right-angled volume, in the absence of a prismatic 4-circuit, we may compute the volume of ideal right-angled polyhedra to be half of the right-angled volume, see Definition 4.4.1. Using this approach, we computed the hyperbolic volumes of right-angled polyhedra with all ideal vertices and compared that to the list by Egorov and Vesnin [23]. Here is the comparison of the first few right-angled volumes by Egorov and Vesnin to the ones generated from our calculations.

Egorov-Vesnin Volumes	Volumes using $vol^{\perp}$	Representative Knot/Link
3.663863	3.663862377	Borromean Link
6.023046	6.023045915	8_{18}
7.327725	7.327724625	9_{40}
8.137885	8.137885205	$K10_{123}$
8.612415	8.6124151	K11a267
9.686908	9.686909425	K11a266
10.149416	10.1494159	K13a4612
10.806002	10.80600241	K12a1188
10.991587	10.99158706	K12a1019
11.136296	11.136298	K12a868
11.447207	11.44720767	K13a3427
11.801747	11.80174705	K14a14867
12.106298	12.10629789	W(3,7)
12.276278	12.27627792	K13a4284

12.414155	12.41415374	K13a3477
12.046092	12.046093005	K13a4695
12.611908	12.6119078	K13a3477
12.854902	12.85490201	K14a14955
12.883862	12.88386202	K13a3478
13.020639	13.02063952	K15a72645
13.310579	13.31057914	K14a17926
13.350771	13.35077051	K14a14858
13.447108	13.44710774	K14a14872
13.677298	13.67729832	K14a16486
13.714015	13.71401469	K15a59989
13.813278	13.81327784	K14a16452
13.907355	13.90735487	K14a16476
14.030461	14.03046101	K14a18208
14.103121	14.10312169	K14a13618
14.160931	14.16092994	K15a81123
14.171606	14.17160624	K15a61083
14.273414	14.27341354	K14a17895
14.469865	14.46986482	K15a64700
14.494727	14.49472755	K15a81002
14.635461	14.63546076	K15a71167
14.655449	14.65544911	K15a81450
14.766948	14.76694873	K15a65728
14.800159	14.80015812	K15a65194
14.832681	14.83268047	K15a82476
14.898794	14.89879438	K15a79628
15.031667	15.0316675	16ah_376571
15.052463	15.05246341	K15a59600
15.07859	15.07858901	16ah_373890
15.11107	15.11106931	K15a65606
15.126498	15.12649826	K15a79577
15.169623	15.16962225	16ah_378852
15.253393	15.25339328	K15a81471

6.2 Maximum $vol^{\perp}$ in class of links with the same number of crossings

We recall that the weaving link $W(m,n)$ has $(m-1)*n$ crossings. We observed the maximum value of right-angled volume in a class of knots and links with the same number of crossings, is almost always achieved by a weaving knot. Note that this applies to crossing numbers which are composite.
The knots from 16 crossings onwards follow the Regina database [5] convention, that is, a knot is represented as c[an][tsh]_k where c denotes the number of crossings, [an] denotes whether is alternating or non-alternating, [tsh] whether the knot is torus, satellite or hyperbolic and k is a positive integer that sorts the knots within each of these classes.

No of Crossings	Knot/Link, $vol^{\perp}$	Weaving Link, $vol^{\perp]}$
8	8_{18}, 12.046091831710571	W(3,4), 12.046146338555
9	9_{40}, 14.655449250122981	W(4,3), 14.6554471764363
10	10_{123}, 16.27577041129425	W(3,5), 16.2756356216559
11	11a266, 19.37381885	NA
12	L12a2008, 24.09218454	W(4,4), 24.0932047926552
13	K13a3478, 25.76772403	NA
14	L14a8699, 29.6653608	No weaving link
15	K15a82477, 32.66314188	W(4,5), 32.5514921226668
16	16ah_379798, 36.13828026	W(5,4), 36.1381695947244
17	17ah_1769978,38.74741933	NA

The absence of a maximum volume weaving knot or link for 14 crossings may be ascribed to the fact that $14 = 2 \times 7$, the weaving parameters are "thin thin" i.e. the ratio p/q is farther away from 1 making it "less squarish" in shape. One direction is to explore the idea that weaving knots or links maximize volumes when p/q is closer to 1.

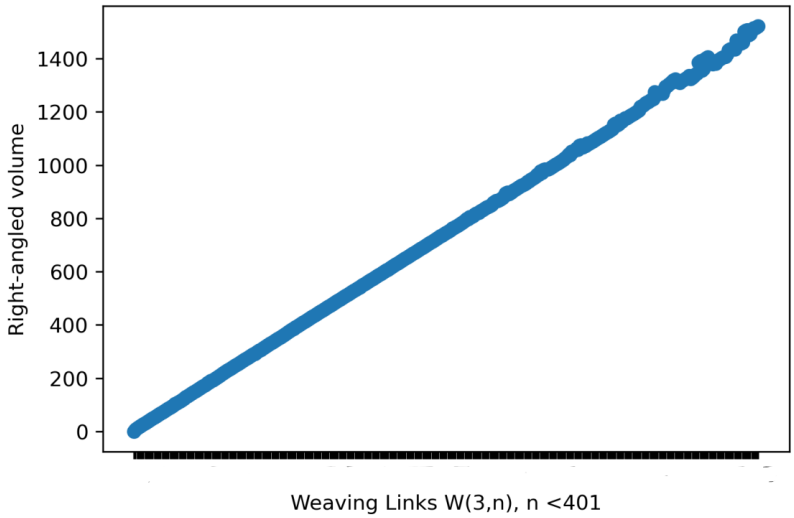

Figure 6.1: Plot of weaving links $W(3, n)$ for $n \leq 400$.

6.3 $vol^{\perp}$ of Weaving links

We computed the right-angled volumes of the weaving links $W(p, q)$ for $3 \leq p \leq 10$ and $3 \leq q \leq 100$, for $p = 3$ and $p = 4$, we have right-angled values for $2 \leq q \leq 400$ and $3 \leq q \leq 200$, respectively.

Upon plotting the data, we observe that $vol^{\perp}$ of $W(p, q)$ is linear in q for a fixed value of p. See Figure 6.1 for the plot of $vol^{\perp}$ of $W(3, n)$ for $n \leq 400$. The regression may be characterized by slope =-2.3541214829762427 with a standard error of 0.5424135406837466 and intercept = 450.9741816998427.

Figure 6.2 is the plot of $vol^{\perp}$ of $W(4, n)$ for $n \leq 200$; the slope of the regression is -1.8505514295689671 with a standard error of 1.1141409345682964 and the intercept is 807.2825230914649.

The plots for $5 \leq p \leq 10$, along with the linear regression parameters can be found here.

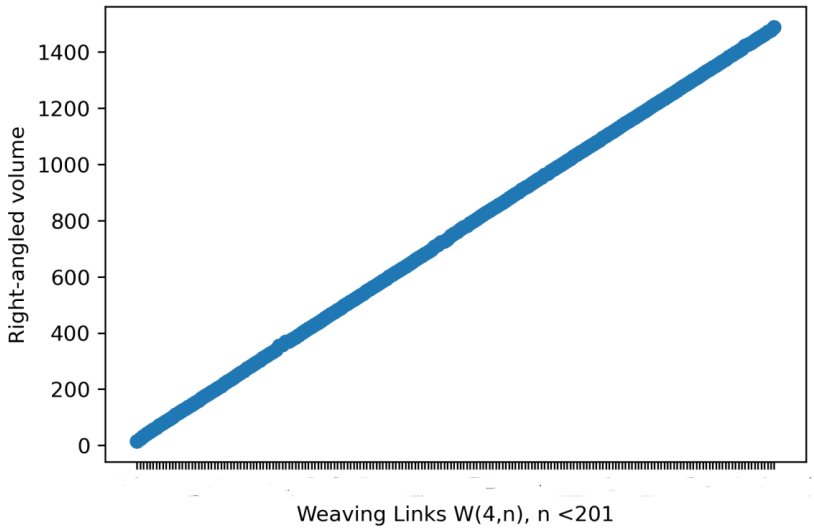

Figure 6.2: Plot of weaving links $W(4, n)$ for $n \leq 200$.

6.4 Right-angled Knots and Links

Definition 6.4.1. *We say that a hyperbolic link L is right-angled if $S^3 - L$ with the complete hyperbolic structure admits a decomposition into ideal hyperbolic right-angled polyhedra. [6]*

Example: Whitehead link and the Borromean link.
Champanerkar Kofman and Purcell in [6] conjectured that there does not exist any right-angled knot. They verified this in [6] for knots up to 11 crossings. This conjecture along with theorem 4.4.1 implies that $vol^{\perp}(K) < vol(K)$. With our new data for the existing census of knots with 17 crossings, we verified that $vol^{\perp}(K) < vol(K)$.
Regarding the existence of right-angled links, we already saw that the whitehead and Borromean links are right-angled. We observed no other links with $vol^{\perp} = vol$ for the link census up to 14 crossings.

6.5 Volume of augmented links

We recall the augmented links and fully augmented links from Definitions 3.2.6 and 3.2.7. We pick an alternating link L with a reduced, twist-reduced, prime alternating diagram. Let

G denote its Tait graph and G' denote its dual Tait graph. Then,

Definition 6.5.1. *We define an alternating link to be fully augmented link-type or FAL-type if either G or G' is a simple, 3-connected and 3-regular graph.*

Using this definition we have obtained a list of fully augmented links and their right-angled volume.

Link	$vol^{\perp}$	3-regularity of G/ G'
L6a4	7.32772475341776	G
9_{40}	14.655449250123	G'
L12a1183	21.9831741056319	G'
K15a65585	29.31083154162286	G'
K15a81477	29.3108757807751	G'
K15a84903	32.5515439799708	G'

Theorem 6.5.1. *Weaving links of type $W(4, m)$ are FAL-type.*

Proof. Consider the weaving link $L = W(4, n)$. Let G denote its Tait graph and V, E the set of all vertices and edges of G respectively. Now, if G is 3-regular, that is $\forall v \in V$, degree of v is 3. As G is 3-connected simple and planar, we have that $3 * |V| = 2|E|$, and hence, $|V|$ is even. Therefore $W(4, m)$ is FAL-type for $m \geq 3$. □

Chapter 7

Conclusion

In this thesis, we extended algorithms and techniques from graph theory to compute the recently defined invariant of alternating knots and links called the *right-angled volume* [6]. We applied our techniques and algorithms to create the first list of right-angled volumes for knots and links in the alternating censuses and extended other similar computations. To summarize:

1. We computed right-angled volumes of knots in the census of alternating knots up to 17 crossings, in total 2,261,298 knots, and of links in the census of alternating links up to 14 crossings, in total 42,183 links.

2. Based on our right-angled volume calculations, we were able to partially recreate the list of volumes of right-angled polyhedra computed by Vesnin and Egorov [23].

3. We computed right-angled volumes of weaving links $W(m, n)$ for $3 \leq m \leq 10$ and $2 \leq n \leq 100$, in total 1,275 weaving links, thereby extending computations in [6].

4. After observing the similarities between our computations and right-angled polyhedral decomposition of fully augmented links, we produced the first list of volumes of fully augmented links.

5. The authors conjecture in [6] that for any alternating hyperbolic knot K, $vol^{\perp}(K) < vol(K)$. Using our computations we verified this conjecture for knots up to 17 crossings.

Our techniques and computations raise interesting questions and open new directions of research. In the future, we would like to explore the following:

1. Extend our tables of right-angled volumes to alternating knots with 18 and 19 crossings.

2. A challenge in computing right-angled volumes of weaving knots and links was the numerical computation of the integral for the Lobachevsky function. We would like to explore other numerical methods for numerical integration and optimizer functions to obtain the calculation of right-angled volume to higher precision, and extend the list of those volumes further.

3. Let L be an alternating link with a reduced, twist-reduced, prime alternating diagram, and let $\mathcal{P}$ denote the associated collection of Andreev polyhedra. It is proved in [6] that $\mathcal{P}$ is an invariant of the L. By definition, the number of essential 4-circuits in the diagram of L is given as $|P|/2 - 1$ and hence is a link invariant. We would like to explore if this invariant can be detected using the polynomial invariant of L e.g. the Alexander or Jones polynomials.

4. Another link invariant obtained from $\mathcal{P}$ is half the total number of ideal vertices of the polyhedra in $\mathcal{P}$. This number is an extension of the twist number of an alternating link. We would like to explore if this invariant can be detected using a polynomial invariant of L e.g. the Alexander or Jones polynomials.

5. In our computations of right-angled volumes of weaving links, we observed that for a fixed crossing number n, sometimes the weaving knot or links maximizes the right-angled volume for that crossing number for e.g. $n = 9$ and sometimes it does not for e.g. $n = 14$. This seems to be related to how close to 1 the maximal ratio of factors of n can be (e.g. if n is a square integer then this ratio is 1). We would like to explore this phenomenon more and investigate if we can prove a precise statement along these lines.

Bibliography

[1] Colin C. Adams. *The knot book*. W. H. Freeman and Company, New York, 1994. An elementary introduction to the mathematical theory of knots.

[2] James W. Anderson. *Hyperbolic geometry*. Springer Undergraduate Mathematics Series. Springer-Verlag London, Ltd., London, second edition, 2005.

[3] Riccardo Benedetti and Carlo Petronio. *Lectures on hyperbolic geometry*. Universitext. Springer-Verlag, Berlin, 1992.

[4] Francis Bonahon. *Low-dimensional geometry*, volume 49 of *Student Mathematical Library*. American Mathematical Society, Providence, RI; Institute for Advanced Study (IAS), Princeton, NJ, 2009. From Euclidean surfaces to hyperbolic knots, IAS/Park City Mathematical Subseries.

[5] Benjamin A. Burton. The next 350 million knots. In *36th International Symposium on Computational Geometry*, volume 164 of *LIPIcs. Leibniz Int. Proc. Inform.*, pages Art. No. 25, 17. Schloss Dagstuhl. Leibniz-Zent. Inform., Wadern, 2020.

[6] Abhijit Champanerkar, Ilya Kofman, and Jessica S Purcell. Right-angled polyhedra and alternating links. *Algebraic & Geometric Topology*, 22(2):739–784, 2022.

[7] Marc Culler, Nathan M. Dunfield, Matthias Goerner, and Jeffrey R. Weeks. SnapPy, a computer program for studying the geometry and topology of 3-manifolds. Available at http://snappy.computop.org (28/08/2023).

[8] Oliver T. Dasbach and Xiao-Song Lin. A volumish theorem for the Jones polynomial of alternating knots. *Pacific J. Math.*, 231(2):279–291, 2007.

[9] Stefan Felsner and Günter Rote. On primal-dual circle representations. In *2nd Symposium on Simplicity in Algorithms*, volume 69 of *OASIcs OpenAccess Ser. Inform.*, pages Art. No. 8, 18. Schloss Dagstuhl. Leibniz-Zent. Inform., Wadern, 2019.

[10] Paul Koebe. *Kontaktprobleme der konformen Abbildung*. Hirzel Stuttgart, 1936.

[11] Charles Livingston and Allison H. Moore. Knotinfo: Table of knot invariants. URL: knotinfo.math.indiana.edu, Current Month Current Year.

[12] A. Marden. *Outer circles: An introduction to hyperbolic 3-manifolds*. Cambridge University Press, Cambridge, 2007.

[13] William W. Menasco. Polyhedra representation of link complements. In *Low-dimensional topology (San Francisco, Calif., 1981)*, volume 20 of *Contemp. Math.*, pages 305–325. Amer. Math. Soc., Providence, RI, 1983.

[14] Edwin E. Moise. *Geometric topology in dimensions* 2 *and* 3, volume Vol. 47 of *Graduate Texts in Mathematics*. Springer-Verlag, New York-Heidelberg, 1977.

[15] Jessica S. Purcell. An introduction to fully augmented links. In *Interactions between hyperbolic geometry, quantum topology and number theory*, volume 541 of *Contemp. Math.*, pages 205–220. Amer. Math. Soc., Providence, RI, 2011.

[16] Jessica S. Purcell. *Hyperbolic knot theory*, volume 209 of *Graduate Studies in Mathematics*. American Mathematical Society, Providence, RI, [2020] ©2020.

[17] Manfred Scheucher. *Program to compute circle packings*. Available at https://page.math.tu-berlin.de/~scheuch/supplemental/primal_dual_circles/.

[18] Alexander Soifer. *The mathematical coloring book*. Springer, New York, 2009. Mathematics of coloring and the colorful life of its creators, With forewords by Branko Grünbaum, Peter D. Johnson, Jr. and Cecil Rousseau.

[19] John Stillwell. *Geometry of surfaces*. Universitext. Springer-Verlag, New York, 1992.

[20] Morwen B. Thistlethwaite. A spanning tree expansion of the Jones polynomial. *Topology*, 26(3):297–309, 1987.

[21] William P. Thurston. Three-dimensional manifolds, Kleinian groups and hyperbolic geometry. *Bull. Amer. Math. Soc. (N.S.)*, 6(3):357–381, 1982.

[22] William P Thurston. *The Geometry and Topology of Three-Manifolds: With a Preface by Steven P. Kerckhoff*, volume 27. American Mathematical Society, 2022.

[23] A. Yu. Vesnin and A. A. Egorov. Ideal right-angled polyhedra in Lobachevsky space. *Chebyshevskiĭ Sb.*, 21(2):65–83, 2020.